Computing numerical solutions for mechanochemical models of developmental growth

Ningyuan CHEN

University of Oxford

This dissertation is submitted for the degree of
Master of Science in Mathematical Modelling and Scientific Computing

Somerville College   September 2019

Acknowledgements

First and foremost, I would like to thank my supervisor, Dr. Ricardo Ruiz Baier and Dr. Matteo Teffanni, to both of whom I am forever grateful for their invaluable advice and direction on this research work. Your timely responses, guidance and dedication helped shape this work. I would also like to thank Dr Kathryn Gillow for her patience and support during this year. A special mention to Jinke He, Boyang Xin, through many hours spent together, have helped me a lot during my studies here. I can never express enough gratitude to my parents. Without them I would surely not be where I am today.

Finally, to Minkun, for being my strength and inspiration in my life.

Abstract

This dissertation proposes a new mechanochemical model for the dynamics of the early stages of mouse limb growth. The governing equations consist of non-linear hyperelasticity written in terms of displacement and solid pressure including growth factors, coupled with a three-species non-linear reaction-diffusion system. Numerical simulations are shown for both isotropic and anisotropic growth, as well as investigating the influence of the boundary condition on the limb outgrowth and shaping. The results are in a good qualitative agreement with the experimentally observed embryonic development of mouse hindlimb from E11.21 to E13.21. Moreover, the inclusion of mechanical feedback on the morphogen dynamics allows the model to reproduce patterns that better mimic the skeletal elements in the limb bud than previously reported results, reinforcing the idea that the interplay between the mechanics and biochemical signalling molecules plays an important role in tissue morphogenesis.

Table of contents

List of figures

Chapter 1

Introduction and Motivation

1.1 Motivation

As listed as one of the most important unsolved problems in developmental biology in a survey conducted by the journal Science in 1994 [31], the actual mechanism for generating a spatial pattern in a developing embryo, known as morphogenesis, has still been mysterious. This major problem has received considerable attention from many different subject areas due to its importance in understanding the origin of life, which has clinical implications for wound healing, tissue regeneration and preventing diseases such as Alzheimer's or cancer.

During morphogenesis, tissues undergo extensive changes in shape, size, and position under the control of genetics, chemistry, and physics. Decades of advancement in molecular biology have led to discoveries in what and how genetic information is translated into biochemical signals that govern body axis determinations, cell differentiation, and tissue patterning in certain morphogenetic events. However, we cannot completely understand morphogenesis through tissue growth by genetic information alone, because deformation and organ development are fundamentally mechanical processes.

From the mechanical perspective, a continuum mechanics approach, which demonstrates an evolving reference configuration and prescribes appropriated constitutive law of growth, has been widely adopted for the analysis of the development of soft tissue. Instability and buckling analysis contribute to understanding the mechanism underlying a wide variety of physiological and pathological phenomena. For example, fingerprint patterns can result from the buckling of the layer of basal cells of the fetal epidermis [24]. However, most work has been established for the growth of the mature soft tissue (such as arterial wall, skin, heart), while relatively less attention has been paid to the embryonic tissue development
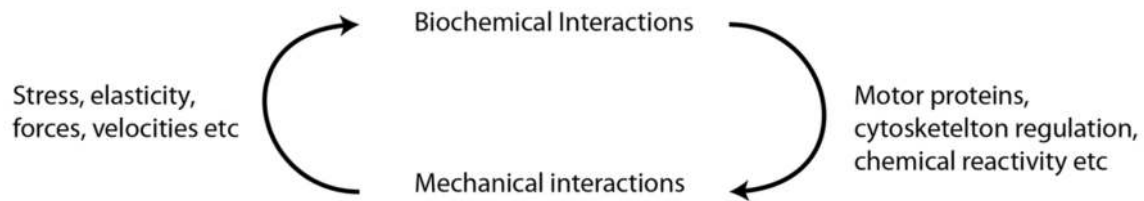
Fig. 1.1 The interdepedency between biochemical reactions and mechanics for Turing patterning. The feedback between components in chemical reactions and mechanical forces is responsible for morphogenesis.

(such as limb, brain) [22]. The limited research in this area might be attributed to the complexities of developing embryonic tissues. In order to understand the complex nature of the morphogenesis, a mechanochemical approach beyond the pure mechanical study is required. Turing [18] described a system undergoing morphogenesis having two states, one mechanical and the other chemical, and explicitly stated that both parts should be taken into account. The philosophy of this mechanochemical approach is to coordinate these two traditionally separate processes. Specifically, the pattern formation of the chemical morphogens and the mechanical forces at the cell and tissue level should act coordinately to generate spatial patterns. The analysis of embryogenic phenomena can proceed as follows: First, focus on the mechanical forces which drive the observed behaviour. Second, the chemistry is added in the way consistent with the observed phenomena so that the resulting mechanochemical model can reproduce the physical pattern stably.

As a practical biological application, we will apply this approach to the early development of the mouse limb as it has long served as a paradigm for studying organogenesis. Before proceeding to the modelling formulation, we will first briefly introduce the mouse limb development and related modelling efforts in the next section.

1.2   Background

We now provide a brief overview of the mouse limb development. This section is not intended to be a comprehensive description; instead, we strive to highlight information that is essential from a modelling perspective, providing insight into the assumptions and choices we make in constructing our model.
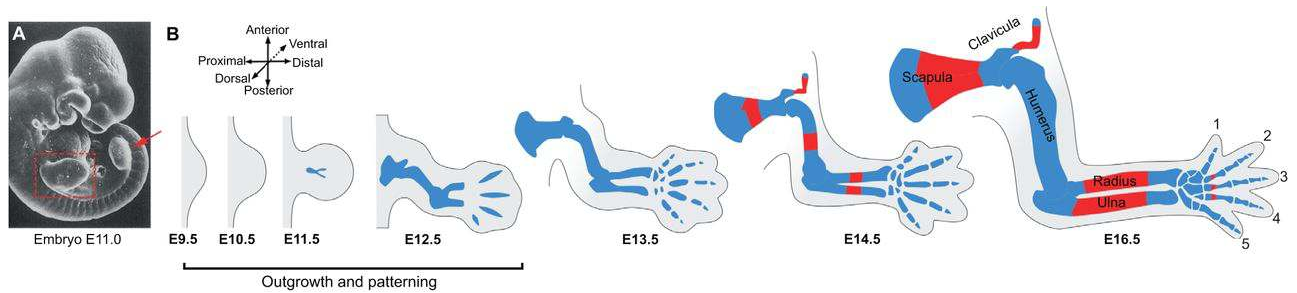
Fig. 1.2 An overview of the stages of limb development. (A) A scanning electron microscopy image of a mouse embryo at E11.0. The forelimb and hindlimb buds are indicated with a red box and a red arrow, respectively. (B) Schematic representations of the morphological changes occurring during forelimb bud development (E9.5-E16.5). Reprinted from [47]

1.2.1 An overview of mouse limb development

A limb has three developmental axes: the **proximo-distal** axes runs from the base of the limb to the tip; the **antero-posterior** axes runs parallel with the body axes (from thumb to the little finger); the **dorso-ventral** axes from the back of the hand to the palm. The mouse is an excellent model to study some aspects of limb development, mainly through spontaneous mutants and artificial know-out [45]. The time scale for describing the age of the embryo is Embryo days EXX (where XX is the number of days from the embryo formation day). Fig 1.2 demonstrates the schematic early-stage development of the mouse limb. The first noticeable sign of limb development are small bulges, called limb buds, emerging from the embryonic body wall around E9.5. As the bud elongates, the mouse limb forms a broad handplate, the cells near the body begin to differentiate into various specialized tissues. By E12.5, the element that makes up the skeleton has formed; they are first formed as cartilage and are later replaced by bone by E14.5. Overall, from the mechanochemical perspective, the limb development can be separated into two major aspects: the outgrowth and the shaping of the limb bud and the pattern formation of skeletal elements.

Limb outgrowth and shaping

The main determinants of limb morphology act at the distal end of the developing limb. The limb bud has two major components: a core of mesenchymal cells, (mesoblast), and an out layer of ectodermal epithelial cells. As the limb bud elongates, a thickened ridge of ectoderm running anteroposteriorly along the limb bud tip, the apical ectodermal ridge (AER) forms and serve as the source of the famous diffusible morphogen, fibroblast growth factor (FGF).
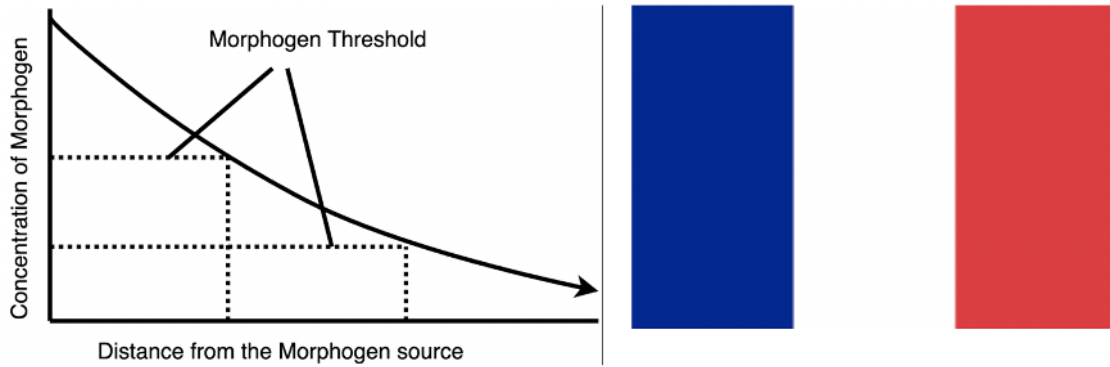
Fig. 1.3 The French Flag model for positional information. The morphogen, expressed from the source forms a gradient, flows left to right, and experience diffusion and decay. Based on [44]

A number of experiments have investigated the effect of the FGFs and showed its essential role in limb outgrowth and shaping. Experiments in the chick wing bud showed that FGF-8 could act as a functional substitute for the apical ectodermal ridge is responsible for the outgrowth [45]. Recent work has shown that FGFs are mitogenic in promoting cell division, and the limb outgrowth depends on the proximal-distal gradient of the FGFs with its maximal value at the distal tip [26]. Previous research also indicated that FGF transforms prospective limb mesoblast into more mechanically active and cohesive material [23, 46].

Skeletal pattern formation

Patterning of the skeletal elements (constituting the main structure) can be attributed to the idea of positional information. The mesenchymal cell differentiation and condensation underlying the pattern formation of cartilage elements are subject to a variety of cellular and molecular interactions [4]. For many decades the standard view has been that the skeletal pattern can be considered as a downstream readout by the cells' genomes of spatial coordinates with respect to the main limb axes, the values of which are specified by graded concentrations of 'positional information' molecules [46]. This view is supported by Wolpert and Hornbruch [44] who established a mathematical model based on a diffusible compound to explain the digit patterning in chick wing. Similar to the idea of French Flag model in Fig 1.3, they suggested the exposure of the cells at different positions to different morphogen concentrations would provide them with the positional value required to form the appropriate digit. This mechanism is referred to as polarizing region signalling involving the morphogen *Sonic hedgehog gene (Shh)* and its source *zone of polarizing activity (ZPA)*. The morphogen Shh was then regarded as the central determinant of positional information [43], but later

research indicated that Shh is a modulator of skeletogenesis rather than part of its core generative mechanism [46]. A recent integrative description of the core signalling pathways that are responsible for gradient systems in the mouse limb development postulates regulatory networks consisting morphogens FGF, Wnt, GLi, Gremlin, BMP, and their receptors [4].

1.2.2   Mathematical modelling in limb development

Most mathematical models for the limb bud development in the literature focused on the skeletal patterning [36, 35, 19, 28]. This might be due to the fact that the establishment and dynamics of the monotonic positional gradients in the position information framework are amenable to mathematical modelling [46]. The physics of self-organizing systems (e.g., Turing-type reaction-diffusion processes) has been frequently employed to understand the emergence of patterns in the limb. The main drawback of these models is usually not solved on realistic growing domains but on static or growing rectangular domains. However, the nature of the patterning and experimental results on the pattern formation of skeletal elements in vivo and in vitro leads to the requirement of studying the patterning on a realistic growing rather than an oversimplified domain [4].

A number of mathematical models have been established to account for the domain growth and changes of the form of free-moving boundaries. Dillon and Othmer [13] presented a continuum mathematical and computational model coupling fluid flow and elastic boundaries to describe limb bud growth in 2D. Growth was coupled to patterning by making the source term dependent on the morphogens' concentration, the dynamics of which are governed by reaction-diffusion–advection equations. This model is the first to integrate tissue growth and the signaling molecule (morphogen) in the context of limb development. In a subsequent 2D treatment, Murea and Hentschel [30] modelled the limb outgrowth as a free boundary problem based on Stokes equation rather than the full Navier-Stokes equation for the high viscosity and low Reynolds number of the mesenchyme.

Numerous studies exploring the limb outgrowth were intended to understand the cellular basis of directional outgrowth. Most of them were based on the idea of 'proliferation gradient,' first described by Ede and Law [14]. Until recently, a model [7] based on the 3D Navier-Stoke equation, supported by new measurements and parameter optimization, indicated that the isotropic proliferation alone is insufficient to explain the changes in shape and size during the limb outgrowth and proposed that directional cell activities are likely to be the driving force behind limb bud outgrowth. Although these efforts advanced the understanding of the cell behaviors and their resulting proliferation rates in the limb outgrowth, the overall picture of

the contribution of the cell proliferation, the orientation of cell divisions and their interplay with cell shape changes and cell rearrangements is still not completely understood [16].

1.3   Goals of this Dissertation

A main recent focus in developmental biology is the experimental identification and mechanochemical modelling of the interplay between the tissue mechanics and biochemical signalling molecules (morphogens) in tissue morphogenesis and patterning in development [8]. The central goal of this thesis is to propose a computational mechanochemical model to reproduce the morphology of embryonic development of mouse hindlimb not only in the very early stage but also after E12 where large deformation on the distal part of the limb bud occurs, as well as underpinning the understanding of the biophysical bases underlying limb development.

From the mechanical perspective, a continuum mechanics approach has been adopted for the analysis of limb growth using the multiplicative decomposition of the deformation gradient for kinematics. From the chemical perspective, we assume that the chemical factors that are thought to influence the growth and motion of the tissue are induced by a key regulatory network, BMP signalling, in the skeletal patterning, which is in turn governed by a set of reaction-diffusion equations. For the coupling, we consider a two-way active transport: the mechanical deformations affect the transport of the chemical species through the change of configuration and also by means of a volume-dependent modification of the reaction terms, and the solutes' concentration generates a scalar growth function affecting the deformation gradients. Very often, these coupled models are of high-dimensions and very non-linear, which impedes to obtain exact solutions in closed form. Therefore, a finite element computational framework is developed and solved using the open-source finite element library FEniCS [2].

The remainder of this thesis is laid out in the following manner. The non-linear elasticity framework is introduced in Chapter 2, coupled with a reaction-diffusion system that has been previously studied for skeletal patterning. A mathematical analysis of the stability of a growing disk is given, as well as the Turing instability for the pattern formation of the reaction-diffusion system. In Chapter 3, we state the weak formulation associated with the coupled system of PDEs and construct a finite element scheme for the discretization of the model equations, using Taylor-Hood finite elements for the displacement-pressure pair and conforming Lagrangian elements for the reaction-diffusion subsystem. We then give a few illustrative numerical examples collected in Chapter 4. These include tests of

Spatio-temporal accuracy verified against manufactured solutions, benchmark computations for the occurrence of the surface instability mechanism in the context of growth-induced instability to exemplify the performance of the mechanical solver, and a few tests of limb growth produced by the proposed coupled multi-physics model. We finalize in Chapter 5 with a summary of our findings and discussion on model extensions.

Chapter 2

Mathematical Model

2.1 Model Formulation

In this section, we describe the formulation of the model for limb-specific morphogenesis. The essential features of our model are a mechanical component modelling limb outgrowth and shaping, and a biochemical component modelling the internal skeletal patterning, coupled through a two-way feedback. We describe the mechanics using theories from non-linear elasticity and continuum mechanics, which are appropriate for describing the large deformations seen during the mouse limb development after E12. We also adopt a reaction-diffusion system governing the key regulatory interaction of morphogens which gives rise to pattern isomorphic to the skeletal element in the limb bud.

2.1.1 Kinematics, motion and deformation

Let $\Omega_0 \subset \mathbb{R}^d$, $d \in \{2,3\}$ denote an elastic body with smooth boundary $\partial\Omega_0$, regarded in its undeformed reference configuration, and denote by ν the outward unit normal vector on $\partial\Omega_0$. We assume a splitting of the boundary $\partial\Omega_0 = \overline{\Gamma_0^D} \cup \overline{\Gamma_0^N}$ into parts Γ_0^D and Γ_0^N where boundary loads and boundary tractions are imposed, respectively. A material point in Ω_0 is denoted by $\mathbf{x}$, whereas $\mathbf{u} : \Omega_0 \to \mathbb{R}^d$ denotes the deformation field that provides its position $\mathbf{x}_t$ within the body Ω_t in the current configuration, and $\hat{\mathbf{v}} = \partial_t \hat{\mathbf{u}}|_{\mathbf{x}}$ is the (referential) velocity.

An important measure of deformation in non-linear continuum mechanics is the deformation gradient tensor defined as $\mathbf{F} := \nabla\mathbf{u}$ (applied with respect to the fixed material coordinates). Its Jacobian determinant, $J = \det\mathbf{F}$ gives the change in volume due to deformation. As strain measures, we choose the Green-Lagrange strain tensor $\mathbf{E}(\mathbf{u}) = \frac{1}{2}[\mathbf{F}^{\mathrm{t}}\mathbf{F} - \mathbf{I}]$. From now on,

the symbols $\nabla_t, \mathbf{div}_t$ will stand for the gradient and divergence operators taken with respect to the spatial coordinates $\mathbf{x}_t$. As usual, $\mathbf{I}$ is the $d \times d$ identity tensor, and we recall that gradient operators in the actual and undeformed configurations are connected by the relation $\nabla_t(\cdot) = \mathbf{F}^{-t} \nabla(\cdot)$.

We concentrate the presentation for non-linear Neo-Hookean materials, whose behaviour can be completely described by the strain (or free energy density) function

$$\Psi\big(\mathbf{F}(\mathbf{u})\big) = \lambda \, \mathrm{tr}\, \mathbf{E} + \frac{\mu}{2} (J(\mathbf{u}) - 1)^2,$$

respectively, where λ, μ stand for the shear and bulk moduli. Focusing on incompressible materials, the first Piola-Kirchhoff stress tensor reads

$$\mathbf{P}(\mathbf{u}, p) = \frac{\partial \Psi}{\partial \mathbf{F}} = 2\mu \mathbf{F} - pJ(\mathbf{u})\mathbf{F}^{-t}.$$

The constitutive equation along with balances of mass and momentum are collected in the following system, written in total Lagrangian formulation

$$\mathbf{P}(\mathbf{u}, p) = \frac{\partial \Psi}{\partial \mathbf{F}} \qquad \text{in } \Omega_0 \times (0, T), \qquad (2.1a)$$

$$J(\mathbf{u}) - 1 = 0 \qquad \text{in } \Omega_0 \times (0, T), \qquad (2.1b)$$

$$\partial_{tt} \mathbf{u} - \mathbf{div}\, \mathbf{P}(\mathbf{u}, p) = \mathbf{f} \qquad \text{in } \Omega_0 \times (0, T), \qquad (2.1c)$$

$$\mathbf{P}\nu = pJ\mathbf{F}^{-T} \mathbf{g_N} \qquad \text{on } \Gamma_0^{\mathrm{N}} \times (0, T), \qquad (2.1d)$$

$$\mathbf{u} = \mathbf{g_D} \qquad \text{on } \Gamma_0^{\mathrm{D}} \times (0, T), \qquad (2.1e)$$

where all differential operators are taken with respect to the reference, material coordinates, and the balance of angular momentum is encoded in the condition

$$\mathbf{P}\mathbf{F}^t = \mathbf{F}\mathbf{P}^t.$$

All this for an isolated, hyperelastic material.

2.1.2 Reaction-diffusion equations in moving and fixed domains

For sake of simplicity we will restrict the discussion to reaction-diffusion systems describing the spatio-temporal interaction of the densities of two species w_1, w_2, however the presentation is straightforwardly generalizable to the case of more species. Assuming that all

constituent species are equi-present at each spatial point, the Reynolds transport theorem applied to the mass conservation of these species yields the following general and non-dimensional reaction-diffusion system for w_1, w_2, w_3 on a spatial (time-dependent) domain

$$\partial_t w_i + \hat{\mathbf{v}} \cdot \nabla_t w_i - \mathbf{div}_t(\mathbf{D}_i \nabla_t w_i) = H_i(w_1, w_2, w_3), \tag{2.2}$$

in $\Omega_t \times (0, T)$, for $i = 1, 2, 3$, where $\mathbf{D}_i \in \mathbb{R}^{d \times d}$ is a tensor of (possibly anisotropic) diffusion rates and $H_i(w_1, w_2, w_3)$ are the reaction kinetics of the system representing the production and degradation of each species concentration. In this particular case, cross-diffusion effects are neglected and the coupling is present only in the reactive terms. Notice that the medium incompressibility has been already incorporated in (2.2) by assuming that $\mathbf{div}_t(\hat{\mathbf{v}} w_i) = \hat{\mathbf{v}} \cdot \nabla_t w_i$. A Lagrangian representation of the domain motion allows to rewrite the target system on a fixed domain in its reference configuration. Pulling back (2.2) to the initial configuration, using the Piola identity $\mathbf{div}(J\mathbf{F}^{-\mathtt{t}}) = 0$, and preliminarily endowing the system with zero-flux boundary conditions, we arrive at

$$\partial_t w_i - \frac{1}{J}\mathbf{div}(J\mathbf{F}^{-1}\mathbf{D}_i\mathbf{F}^{-\mathtt{t}}\nabla w_i) = H_i(w_1, w_2, w_3) \qquad \text{in } \Omega_0 \times (0, T), \text{ for } i = 1, 2, 3,$$
$$J\mathbf{F}^{-1}\mathbf{D}_i\mathbf{F}^{-\mathtt{t}}\nabla w_i \cdot v = 0 \qquad \text{on } \partial\Omega_0 \times (0, T), \text{ for } i = 1, 2, 3. \tag{2.3}$$

2.1.3 Pattern formation and limb morphogenesis

We now focus on the modeling of organogenesis based on simple reaction-diffusion systems governing the interaction between bone morphogenic proteins (BMP) and fibroblast growth factors concentration (FGF). In [4] the authors developed a three-species model of mouse limb where the growth velocity of the tissue is prescribed normal to the limb surface and directly depends on the local concentration of fibroblast growth factor. Other models consider the tissue growth as a liquid displacement [30, 7, 13], or it is typically assumed that the position of the cell aggregates can be computed as a postprocess of some growth factor [27]. However, evidence shows that its short-term response corresponds with that of an elastic solid [13], and therefore here we assume that the domain can deform according to its inherent mechanical response, and that it is affected isotropically by a scalar-valued internal variable associated with the addition/subtraction of mass, which is defined in terms of the growth rate and will be prescribed shortly.
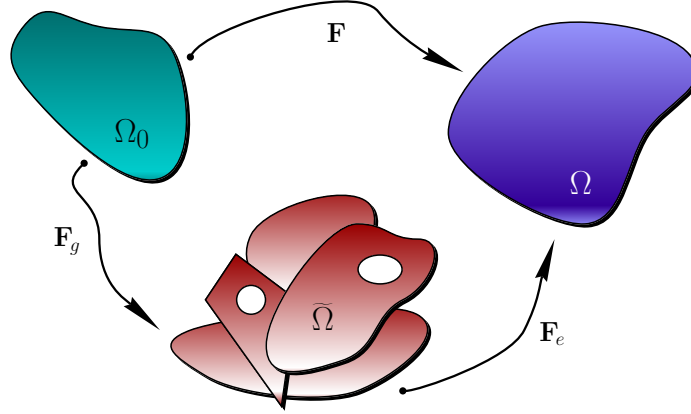
Fig. 2.1 Multiplicative decomposition of deformation gradient Decompose $\mathbf{F}$ into pure growth $\mathbf{F}_g$ and an elastic deformation tensor $\mathbf{F}_e$. The intermediate configuration $\widetilde{\Omega}$, between the undeformed reference state Ω_0 and the current/final configuration Ω including growth and elastic response with stress, is an incompatible virtual and stress-free growth state.

Multiplicative decomposition of deformation gradient tensor

The way that this coupling term enters the constitutive equations occurs due to a decomposition of the deformation mapping into a purely growth part and the remainder, elastic, deformation. Such splitting implies that there exists an intermediate configuration $\widetilde{\Omega}$ between Ω_0 and Ω which is not necessarily compatible (and which we assume is completely stress free, see sketch in Figure (2.1), and consequently a multiplicative decomposition of the deformation gradient into a growth deformation gradient (describing local generation or removal of material points) and an elastic deformation gradient tensor is admitted (see for instance [22, 40])

$$\mathbf{F} = \mathbf{F}_e \mathbf{F}_g, \tag{2.4}$$

where $\mathbf{F}_e$ and $\mathbf{F}_g$ are the growth deformation gradient and elastic deformation gradient respectively.

Elastic deformation gradient and stress tensor

Since the intermediate configuration is considered stress-free, stresses are exerted only by the elastic deformation, and the constitutive relations between a given strain energy function Ψ (that characterises the material response of the solid for hyperelastic materials) and the measures of stress (in this case, the first Piola-Kirchhoff tensor) can be stated with respect to the intermediate configuration $\widetilde{\Omega}$

$$\mathbf{P}_e = \frac{\partial \Psi}{\partial \mathbf{F}}\big|_{\tilde{\Omega}}, \tag{2.5}$$

This is more clearly seen if one defines an augmented energy density functional associated with

$$\widetilde{\Psi}\left(\mathbf{F},\mathbf{F}_g\right) = J_g\Psi\left(\mathbf{F}\mathbf{F}_g^{-1}\right) - p\left(J_e - 1\right),$$

where $J_g := \det\mathbf{F}_g$ is the local change of volume due to growth, and $J_e := \det\mathbf{F}_e$ is the reversible part of the Jacobian[1]. Assuming that the material behaves as a Neo-Hookean solid, equations (2.4)-(2.5) imply that

$$\mathbf{P}_e = J(\mu\mathbf{B}_e - p\mathbf{I})\mathbf{F}^{-\mathtt{t}},$$

where μ is the shear modulus of the Neo-Hookean material, p denotes the solid pressure acting as Lagrange multiplier, and the right Cauchy-Green deformation tensor $\mathbf{B}_e$ associated with the intermediate configuration $\widetilde{\Omega}$ is defined as

$$\mathbf{B}_e = \mathbf{F}_e\mathbf{F}_e^{\mathtt{t}},$$

Note that in this context, rather than material incompressibility, the Lagrange multiplier enforces a constraint on the reversible part of the Jacobian $J_e := \det\mathbf{F}_e = \det(\mathbf{F}\mathbf{F}_g^{-1}) = 1$, implying an elastically incompressible material: all volume changes are solely due to growth factors ($J_g = \det\mathbf{F}_g$ is in turn irreversible).

Then, stated in the reference configuration, the equations of non-linear elasticity with growth (including momentum conservation of the solid and the incompressibility of elastic deformations) read as follows

$$\partial_{tt}\mathbf{u} - \mathbf{div}\left(\mathbf{P}_e\right) = \mathbf{0} \qquad\qquad \text{in } \Omega_0 \times (0, t_{\text{final}}], \qquad\qquad (2.6)$$

$$J_e = 1 \qquad\qquad \text{in } \Omega_0 \times (0, t_{\text{final}}], \qquad\qquad (2.7)$$

where the divergence and gradient operators are understood with respect to the undeformed coordinates.

Growth deformation gradient tensor

It remains to characterise the growth deformation gradient. We suppose that growth occurs due to a growth factor r acting isotropically in the undeformed configuration, and so a general form for the growth deformation tensor is simply

$$\mathbf{F}_g = r\mathbf{I},$$
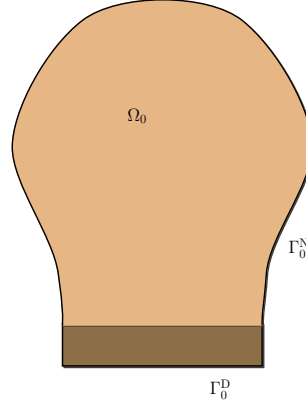
Fig. 2.2 Schematic representation of the computational domain. Modelling an unde-formed idealized Mouse limb bud, and indicating specific parts of the boundary.

In this case, r represents the stretch ratio due to volumetric change. However other more general descriptions including anisotropy could be formulated, e.g.

$$\mathbf{F}_g = \mathbf{I} + r_1 \mathbf{d}_1 \otimes \mathbf{d}_1 + r_2 \, \mathbf{d}_2 \otimes \mathbf{d}_2,$$

where r_1, r_2 dependent on r and $\mathbf{d}_i$ are specific directions of prescribed growth in the reference configuration and the identity indicates that the growth factors should be compared with 0 instead of 1.

Evolution law of internal scalar growth factor r

To completely characterize a constitutive law for the growth, a complementary law is required. That is the evolution of r must be postulated. We assume that the motion of the body is influenced by growth factor defined as

$$r = \gamma w_1 w_2^2, \tag{2.8}$$

where γ is a growth amplifying factor depending only on time, w_1 is BMP and w_2 is the BMP receptor. Here we assume the pattern formed by BMP-receptor complex, $w_1 w_2^2$, resembling the final digit structure inside the limb bud, drives the isotopic or anisotropic growth. The concentrations of morphogen bone morphogenic proteins w_1, its receptor w_2 and fibroblast growth factors w_3 results from a complex regulatory interaction, BMP signalling, which is govern by a non-dimensional Schnakenberg-type Turing mechanism proposed by [4] and its reaction terms are
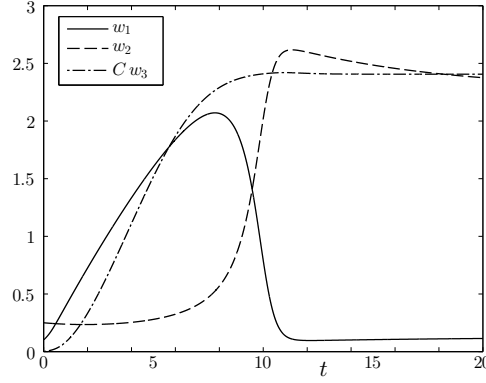
Fig. 2.3 Dynamics of the morphogen w_1**,** w_2**, (and rescaled)** w_3 **at a point.** Computed according to the kinetics of the model described in (2.9).

$$H_1(w_1,w_2,w_3) = \underbrace{\rho_1 + \rho_1^* \frac{w_3^2}{(1+w_3^2)(1+w_2^2 w_1)}}_{\text{production}} - \underbrace{\delta_c w_2^2 w_1}_{\text{complex formation}} - \underbrace{\delta_1 w_1}_{\text{degradation}},$$

$$H_2(w_1,w_2,w_3) = \underbrace{\rho_2}_{\text{production}} + \underbrace{(\nu - 2\delta_c)w_2^2 w_1}_{\text{complex formation}} - \underbrace{\delta_2 w_2}_{\text{degradation}}, \qquad (2.9)$$

$$H_3(w_1,w_2,w_3) = \underbrace{\rho_3 \frac{k_2^2 w_2^4 w_1^2}{(k_1^2 + w_2^4 w_1^2)(k_2^2 + w_2^4 w_1^2)}}_{\text{production}} - \underbrace{w_3}_{\text{degradation}},$$

where the chosen parameters are

$$\rho_3 = 243.1, \quad \rho_2 = 0.0145, \quad \nu = 1.361, \quad \rho_1^* = 12\rho_2,$$
$$\rho_1^a = 0.063, \quad \rho_1^b = 3\rho_1^a, \quad \delta_2 = 0.135, \quad \delta_1 = 0.15\delta_2,$$
$$\delta_c = \nu/3, \quad k_1 = 0.06588, \quad k_2 = 50000, \qquad (2.10)$$
$$\gamma = 2.5\mathrm{e}-6(t > 250), \rho_1 = (y > y_0)\rho_1^a + (y \le y_0)\rho_1^b.$$

We choose this Schnakenberg Turing-type model because it is one of the simplest models which contains the minimal essential factor of BMP signaling based on a biological realistic domain and can be used to obtain patterns of BMP-receptor activity that resemble the experimentally observed marker for digit condensation. It simply describes the interaction between BMP, its receptor and an important modulator and growth factor FGF. For more details regarding this reaction-diffusion system we refer the reader to reference [4]. The

dynamics of these reactions in a short time horizon are depicted in Figure (2.3). The receptor (w_2) slowly increases until the BMP (w_1) are reaching a peak, followed by an abrupt replacement of species w_2 and w_1. The growth of FGF (w_3) persists until reaching its maximum.

The undeformed geometry representing an idealized limb bud is sketched in the right panel of Figure 2.3, where we distinguish between the apical ectodermal ridge Γ_0^{N} (the tip of the limb bud, on which stress free conditions will be applied) and the stalk Γ_0^{D} (where we impose zero displacements). Zero-flux boundary conditions are set for w_1, w_2 everywhere, whereas instead of the specification in ((2.3)), a production of w_3 is assumed on the apical ectodermal ridge according to

$$\mathbf{D}_3 \nabla w_3 \cdot v = H_3(w_1, w_2, w_3) + \delta_3 w_3, \quad \text{on } \Gamma_0^{\mathrm{N}},$$

with $\delta_3 = 1.01$.

2.1.4 Summary of governing equations

Now, we summarize the equations governing the limb development

Multiplicative decomposition	$\mathbf{F} = \mathbf{F}_e \mathbf{F}_g,$	(2.11)
Momentum conservation	$\partial_{tt}\mathbf{u} - \text{div}(\mathbf{P}_e) = \mathbf{0},$	(2.12)
Incompressibility condition	$J_e = 1,$	(2.13)
Constitutive relation	$\mathbf{P}_e = \left.\dfrac{\partial \Psi}{\partial \mathbf{F}}\right|_{\widetilde{\Omega}} = J\left(\mu\mathbf{B}_e - p\mathbf{I}\right)\mathbf{F}^{-t},$	(2.14)
Growth deformation	$\lambda\,\mathbf{F}_g = \mathbf{I} + r_1\mathbf{d}_1 \otimes \mathbf{d}_1 + r_2\mathbf{d}_2 \otimes \mathbf{d}_2,$	(2.15)
Reaction-diffusion	$\partial_t w_i - \text{div}\left(\mathbf{F}^{-1}\mathbf{D}_i\mathbf{F}^{-t}\nabla w_i\right) = H_i\left(w_1, w_2, w_3\right),$	
	$i = 1, 2, 3,$	(2.16)

subject to the boundary conditions

$$
\begin{aligned}
\mathbf{u} &= \mathbf{0} & &\text{on} \quad \Gamma_0^{D}, \\
\mathbf{P_e m} &= J\mathbf{F}^{-t}\mathbf{t} & &\text{on} \quad \Gamma_0^{\mathrm{N}}, \\
\mathbf{F}^{-1}\mathbf{D}_i\mathbf{F}^{-t}\nabla w_i \cdot v &= 0, \; i = 1, 2 & &\text{on} \quad \Gamma_0^{\mathrm{N}} \cup \Gamma_0^{D}, \\
\mathbf{D}_3 \nabla w_3 \cdot v &= H_3\left(w_1, w_2, w_3\right) + \delta_3 w_{3,} & &\text{on} \quad \Gamma_0^{\mathrm{N}}.
\end{aligned}
\tag{2.17}
$$

The diffusion tensors for all morphogens are taken isotropic $\mathbf{D}_i = D_i\mathbf{I}$ with $D_1 = 2.7, D_2 = 0.01D_1, D_3 = 1$. The material parameter is $\mu = 12$ (no need for λ in the incompressible case).

We now have a system of coupled partial differential equations. As it would be extremely difficult to obtain analytical solutions, we would need to solve the system numerically to obtain approximate solutions. In this thesis, we make use of finite element method to find such approximate solutions. One can use a Taylor-Hood discretisation for displacement and pressure of the solid, and Lagrangian (continuous and piecewise linear approximations) for the chemical species. A fixed time step of $\Delta t = 0.05$ can be employed and starting from the nonzero initial data $w_1(0) = w_3(0) = 0.1, \mathbf{u}(0) = 0$ and a uniformly distributed random perturbation around 0.25 for w_2, the system has to be evolved until roughly $T = 2500$, where pseudo-stationary spatial profiles start to emerge.

2.1.5   Computational domain

A crucial feature of our model is that its computational domain has similar shape as the limb. Rather than a simple mathematically defined 'bulging' shape, we wish to use more physiological accurate shape features. Therefore, the shape of the domain was extracted from limb bud images at E11.5 from [25]. The limb bud is split into hand plate and stalk. The ratio of dimensions of various surfaces in both the handplate and stalk of the limb bud is extracted. Importing these data, we used an open-source finite element grid generator, Gmsh [15], to construct the 2D geometric representation of the model and generate the unstructured triangular meshes.
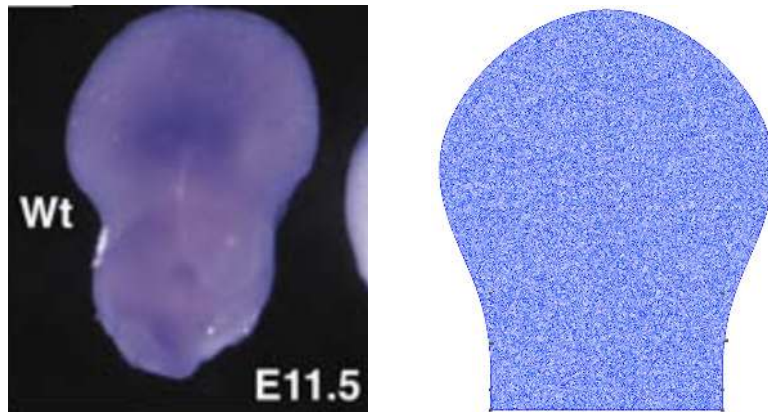
Fig. 2.4 Computational domain. Left: the shape of the mouse limb on E11.5, reprinted from [25]. Right: idealized geometry and mesh generated from Gmsh.

2.2   Analysis of the model

In this section, we want to gain more insight into the stability and pattern formation mechanism behind the proposed model. Therefore, we will separate the full coupled model into two subparts and perform some analysis on each of them with appropriate simplifications.

2.2.1   Residual stress in a fixed disk

In many biological tissues, the generation of residual stress through differential growth is a critical feature of any mechanical theory of growing bodies. In this section, we aim to answer the question: whether / how the differential growth in our growing limb model could induce the compressive stress (circumferential direction particularly)? In order to answer this, we present a toy problem of a growing two-dimensional incompressible, hyperelastic solid disk representing the deformation of handplate resulting from both isotropic and anisotropic growth process. The geometry is sketched in Fig (2.5). Similar analyses have been widely performed in the context of the growth and remodelling of soft tissue e.g., [39].

Assume the disk is fixed at its centre and the growth tensor to be of the form $\mathbf{F}_g = \mathrm{diag}(g_r, g_\theta)$, where g_r, g_θ are the growth ratios in the radial and circumferential directions. Consider an element of the tissue, at distance R from the axis of the disk in the stress-free state before the growth. The element moves to a place at distance r from the axis of the disk after the growth. The function $r(R)$ specifies the field of displacement. By applying the multiplicative decomposition of the deformation gradient $\mathbf{F} = \mathbf{F}_e \mathbf{F}_g$, the elastic deformation tensor can be extracted

$$\mathbf{F}_e = \mathrm{diag}(\lambda_r, \lambda_\theta), \tag{2.18}$$

where the principal stretches are given by

$$\lambda_r = g_r^{-1} \frac{\partial r}{\partial R}, \quad \lambda_\theta = g_\theta^{-1} \frac{r}{R}. \tag{2.19}$$

Then the incompressibility condition, namely $\det(\mathbf{F}_e) = 1$, implies that the deformation is determined by the equation

$$\frac{\partial r}{\partial R} = \frac{R}{r} g_r g_\theta. \tag{2.20}$$

After integration this yields

$$r^2 = g_r g_\theta R^2, \tag{2.21}$$
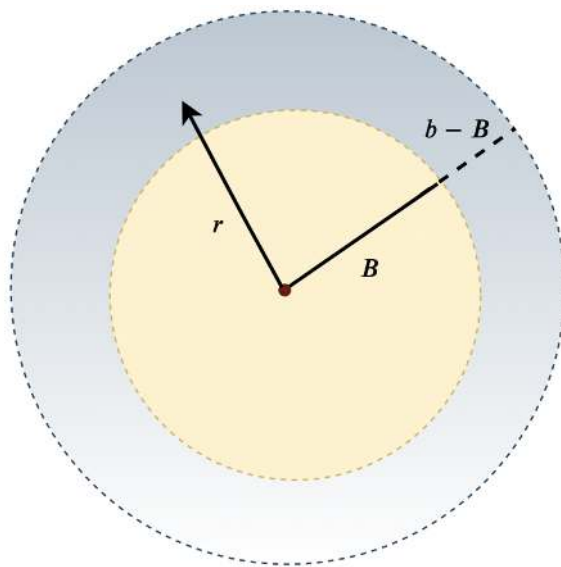
Fig. 2.5 The deformation of a fixed disk under the plain-strain condition. *B* is the radii of the fixed disk before the growth and *b* is the radii in the stressed state after the growth; *r* specifies the the field of displacement of any stress-free element after the growth.

where we use the condition that the disk is fixed at its centre. Substituting (2.20) and (2.21) into (2.19), we have

$$\lambda_r = (\frac{g_\theta}{g_r})^{1/2}, \quad \lambda_\theta = (\frac{g_r}{g_\theta})^{1/2}. \tag{2.22}$$

Let $\sigma_{rr}, \sigma_{\theta\theta}$ be the radial and circumferential stress of the Cauchy stress tensor. In the absence of body forces, the equilibrium linear momentum equation is $\text{div}\,\sigma = 0$ and the only non-zero components of Cauchy stress tensor satisfying

$$\frac{\partial \sigma_{rr}}{\partial r} + \frac{\sigma_{rr} - \sigma_{\theta\theta}}{r} = 0, \tag{2.23}$$

where

$$\sigma_{rr} = \mu\lambda_r^2 - p, \quad \sigma_{\theta\theta} = \mu\lambda_\theta^2 - p.$$

Assuming there is no stress on the outer boundary, integrating (2.23) from the outer radii *b* to *r*, we have

$$\sigma_{rr}(r) = \int_b^r \frac{\sigma_{\theta\theta}(s) - \sigma_{rr}(s)}{s} ds.$$

The stress components can be further written as

$$\sigma_{rr}(r) = \mu \int_b^r \frac{g_r^2 - g_\theta^2}{g_\theta g_r s} ds, \tag{2.24}$$

$$\sigma_{\theta\theta}(r) = \sigma_{rr} + \mu \frac{g_r^2 - g_\theta^2}{g_\theta g_r}. \tag{2.25}$$

Here we obtain the stress in terms of the growth rate. In the isotropic case ($g_r = g_\theta$), we can see that $\sigma_{rr} = \sigma_{\theta\theta} = 0$ and so there is no residual stress in the disk; In the anisotropic case, if the growth is homogeneous, the stress in the radial direction can be extracted

$$\sigma_{rr}(r) = \mu \frac{g_r^2 - g_\theta^2}{g_\theta g_r} \log(\frac{r}{b}), \tag{2.26}$$

$$\sigma_{\theta\theta}(r) = \mu \frac{g_r^2 - g_\theta^2}{g_\theta g_r} (\log(\frac{r}{b}) + 1). \tag{2.27}$$

It can be noted that $\log(r/b) < 0$ since $r/b < 1$. This implies the occurrence of compressive stress that could give rise to the instability depends upon the sign of $g_r - g_\theta$ and $1 + \log(r/b)$.

2.2.2 Pattern formation by Turing instability

Recall that the governing non-dimensional equation for the regulatory interaction of three chemical species is

$$\partial_t w_1 + \hat{\mathbf{v}} \cdot \nabla_t w_1 - D_1 \Delta_t w_1 = \rho_1 + \rho_1^* \frac{w_3^2}{(1 + w_3^2)(1 + w_2^2 w_1)} - \delta_c w_2^2 w_1 - \delta_1 w_1, \tag{2.28}$$

$$\partial_t w_2 + \hat{\mathbf{v}} \cdot \nabla_t w_2 - D_2 \Delta_t w_2 = \rho_2 + (v - 2\delta_c) w_2^2 w_1 - \delta_2 w_2, \tag{2.29}$$

$$\partial_t w_3 + \hat{\mathbf{v}} \cdot \nabla_t w_3 + \Delta_t w_3 = \rho_3 \frac{k_2^2 w_2^4 w_1^2}{(k_1^2 + w_2^4 w_1^2)(k_2^2 + w_2^4 w_1^2)} - w_3, \tag{2.30}$$

in $\Omega_t \times (0, T)$, for $i = 1, 2, 3$. Here we assume zero-flux boundary condition.

Linear stability analysis

The first step in linear stability analysis is to find the base state in which the solution is time-independent. A simple choice is to let $\hat{\mathbf{v}}_0 = 0$ and find three constants $w_{1,0}, w_{2,0}, w_{3,0}$ such that

$$H_i(w_{1,0}, w_{2,0}, w_{3,0}) = 0, \qquad i = 1, 2, 3.$$
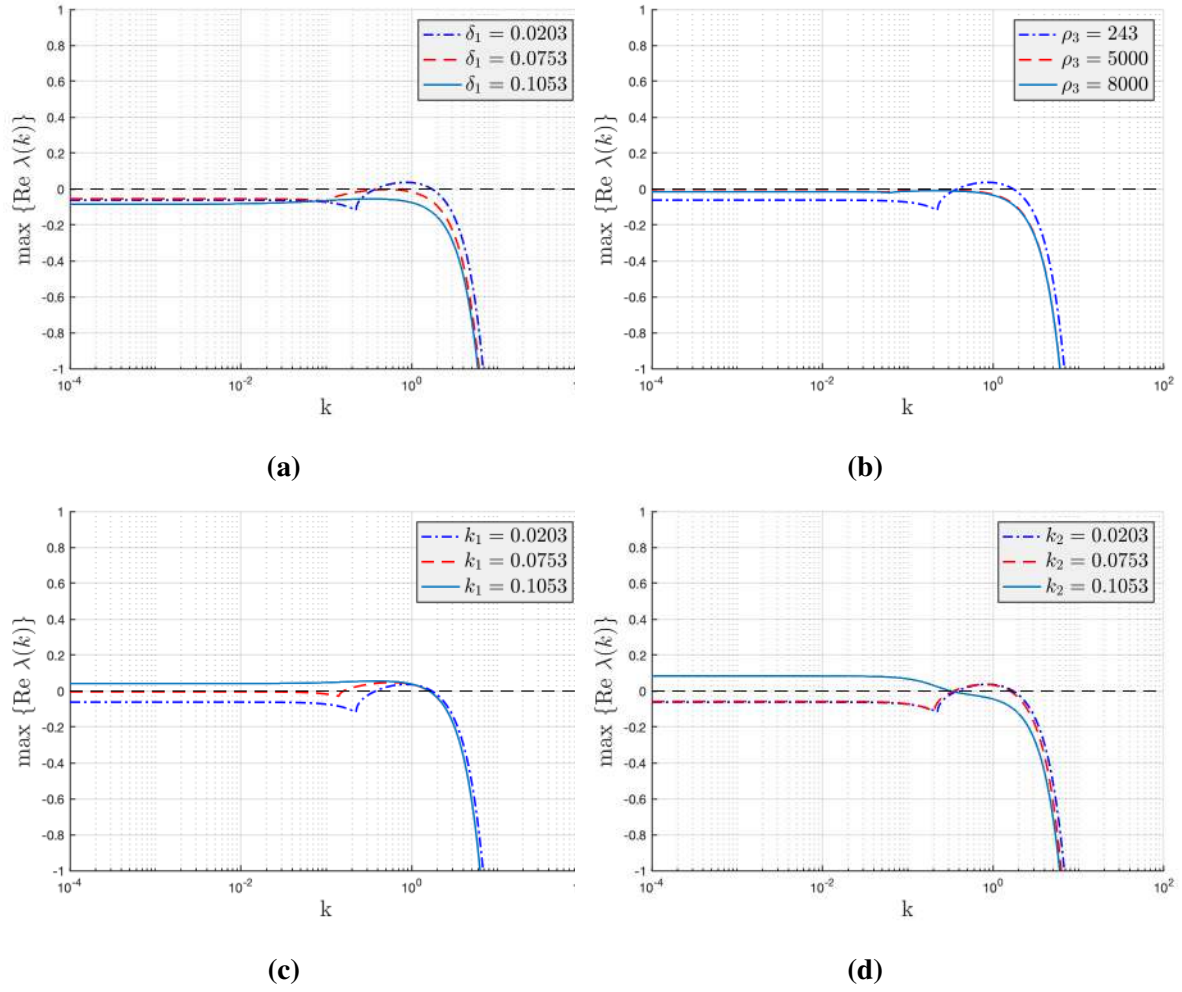
Fig. 2.6 Dispersion relation curves for a reaction-diffusion system with kinetics defined in (2.9)**.**

We now subject the base state to a small perturbation. Let us consider an infinitesimal perturbation of the basic flow velocity of the chemical species due to domain evolution

$$\hat{\mathbf{v}} = \hat{\mathbf{v}}_0 + \varepsilon \hat{\mathbf{v}}_1, \tag{2.31}$$

where $|\varepsilon| \ll 1$, so that the term $\hat{\mathbf{v}}_1$, can be regarded as a first order incremental flow velocity with respect to the equilibrium. Similarly, considering the equilibrium state $w_{i,0}, i = 1, 2, 3$ of chemical species $w_i, i = 1, 2, 3$ associated with the perturbation, which writes

$$w_i = w_{i,0} + \varepsilon w_{i,1}, i = 1, 2, 3 \tag{2.32}$$

Substitute (2.31) and (2.32) into the governing equation and expand these equations about the base state in the increasing powers of the perturbation's amplitude ε. Neglecting terms $O\left(\varepsilon^2\right)$ and higher, we obtain the following set of equations governing the dynamics of the perturbation

$$\partial_t \mathbf{w}_1 = \mathbf{D}\Delta_t \mathbf{w_1} + \mathbf{J}\mathbf{w_1}, \tag{2.33}$$

where $\mathbf{w_1} = (w_{1,1}, w_{2,1}, w_{3,1})^T, \mathbf{D} = \mathrm{diag}(D_1, D_2, D_3), \mathbf{J} = [J_{ij}] = [\frac{\partial H_i}{\partial w_j}(w_{1,0}, w_{2,0}, w_{3,0})]$. The linearised equations are further study studied via a normal mode analysis. Consider the related eigenvalue problem with zero-flux boundary condition

$$\Delta_t \mathbf{w} + k^2 \mathbf{w} = 0,$$

where the eigenfunction can be derived as $\mathbf{w} = e^{\mathbf{k}\mathbf{x}i}$ (Here i is the imaginary number and $\mathbf{k} = (k_1, k_2)$ $(k_1, k_2$ are discrete) is the wave vector with magnitude $k^2 = (k_1)^2 + (k_2)^2$. Since the problem is linear, the first order increment of the solution in terms of a spectral decomposition in the form

$$\mathbf{w}_1(\mathbf{x}, t) = \sum_j \mathbf{c_j}\mathbf{w^{k_j}}((\mathbf{x}))e^{\lambda_j t} = \sum_j c_j.e^{\mathbf{k_j}\mathbf{x}i}e^{\lambda_j t},$$

where c_k is the coefficient of the Fourier expansion. It should be noted that the spatial part is governed by the wave modes $\mathbf{w^{k_j}}(\mathbf{x})$ with wave number $\mathbf{k}_j$ and the temporary part is determined by the corresponding eigenvalue λ_j. Substituting the separation of the form $\mathbf{w}(\mathbf{x})e^{\lambda t}$ into (2.33), the original linearised problem translates into

$$\mathbf{M} = \left(\lambda \mathbf{I} + k^2 \mathbf{D} - \mathbf{J}\right)\mathbf{w} = 0.$$

We then proceed to obtain the dispersion relation $\lambda(k)$ associated with the characteristic polynomial $\det(\mathbf{M})$. Unless specified otherwise, we will employ the parameter values provided in (2.10). The occurrence of Turing instability (pattern formation) requires the steady state is stable without spatial variation ($k^2 = 0, \mathrm{Re}\,\lambda < 0$) and the system become unstable with spatial variation ($\exists k \neq 0, \mathrm{Re}\,\lambda(k) > 0$). This condition is portrayed in the dispersion relation curve presented in Fig 2.6 (a)-(d) and we demonstrate how the dispersion relation curves vary with the regulation parameter k_1, k_2, decay rate δ_1, production rate ρ_1. It can be noted that these parameters has a particular wide parameter range where the pattern will emerge; We can also notice that the critical wave number is always one, indicating where the unstable pattern modes will grow.

The Turing space for diffusion-driven spatial instability in terms of the other parameters in the model system is shown in Fig 2.7. Based on these two plots, we can determine in what
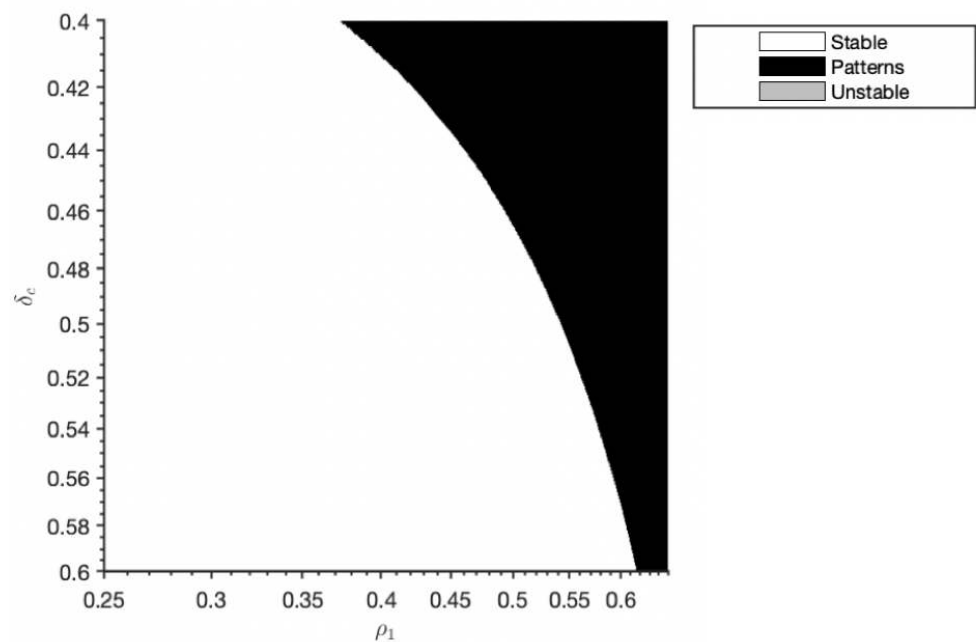
(a)
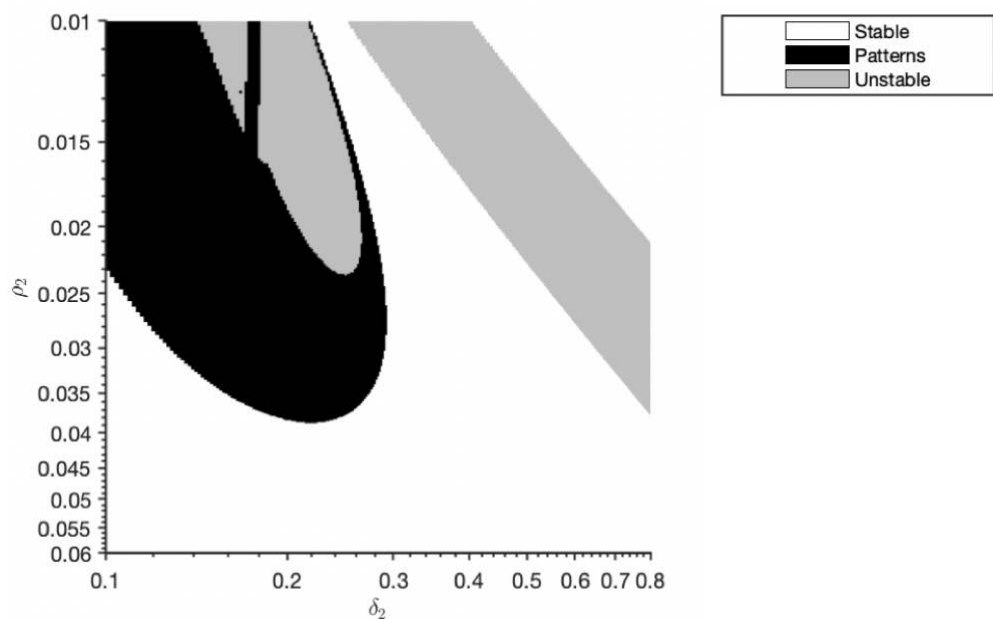
(b)

Fig. 2.7 Turing pattern analysis for a reaction-diffusion system with kinetics defined in (2.9) (a),(b) Bifurcation diagrams.

parameter regions patterns are possible. However, we do not know at this point what patterns

to expect, but only that spatial patterns are possible. To go further and determine which type of patterns will emerge, a weakly non-linear analysis is needed.

Chapter 3

Numerical Methods

In this Chapter, we describe the numerical method used to produce approximate solutions to our model. We choose to work with primal-mixed finite element methods similarly to what is advanced in [41, 11]. The term primal indicates that the method targeting the solution of the equations describing moprhogens interactions solve for chemical concentrations only. On the other hand, the term mixed refers to the simultaneous approximation of different physical quantities, which is beneficial in that it respects the structure of our governing equations in the mechanical system solving for both displacement and pressure. Another advantage is that the formulation imposes more adequately the non-linear constraint of incompressibility of the elastic deformations, avoiding the phenomenon of volumetric locking. The time discretization is carried out using simply central and one-sided differences to approximate second and first order derivatives, and the solution of the non-linear systems arising at each time step is conducted by means of the Newton-Kantorovich iterative algorithm.

3.1   Deriving a weak formulation

From now on, standard notation will be adopted for Lebesgue spaces $\mathrm{L}^p\left(\Omega_0\right)$. We recall the definition of the vectorial Sobolev space vectorial Sobolev spaces

$$\mathbf{W}_{\mathrm{D}}^{1,4}\left(\Omega_0\right) = \left\{\mathbf{v} \in \mathbf{W}^{1,4}\left(\Omega_0\right) : \mathbf{v}|_{\Gamma^{\mathrm{D}}} = g_{\mathrm{D}}\right\},$$

and its restriction

$$\mathbf{H}_{\mathrm{D},0}^{1}\left(\Omega_0\right) = \left\{\mathbf{v} \in \mathbf{H}^{1}\left(\Omega_0\right) : \mathbf{v}|_{\Gamma^{\mathrm{D}}} = \mathbf{0}\right\},$$

which will serve, respectively as trial and test functional spaces for dis- placements. Multiplying the non-linear, coupled equations (2.6) and (2.7) by suitable test functions, integrating by parts over Ω_0, we arrive at the following variational form of the model problem with Neo-Hookean elasticity: *For any $t > 0$, Find $(\mathbf{u}(t), p) \in \mathbf{W}_D^{1,4}(\Omega_0) \times L^2(\Omega_0)$ satisfying*

$$\int_{\Omega_0} \partial_{tt}\mathbf{u} \cdot \mathbf{v} + \int_{\Omega_0} \mathbf{P_e} : \nabla\mathbf{v} = \int_{\Gamma_0^N} J\mathbf{F}^{-t}\mathbf{t} \cdot \mathbf{v},$$
$$\int_{\Omega_0} (J_e - 1)q = 0,$$
(3.1)

for all $(\mathbf{v}, q) \in \mathbf{H}_{D,0}^1(\Omega_0) \times L^2(\Omega_0)$. For sake of conciseness of the presentation, we will also introduce the non-linear operators

$$[\mathscr{A}(\mathbf{u}, p), \mathbf{v}] := \int_{\Omega_0} \mathbf{P}_e : \nabla\mathbf{v}, \qquad [\mathscr{B}(\mathbf{u}), q] := \int_{\Omega_0} (J_e - 1)q,$$
$$[\mathscr{G}(\mathbf{u}), \mathbf{v}] := \int_{\Gamma_0^N} J\mathbf{F}^{-t}\mathbf{t} \cdot \mathbf{v}.$$

Similarly, for the reaction-diffusion system in the undeformed coordinates (2.2) we test the three equations against smooth functions, integrate by parts over Ω_0 on the high-order terms, and put the resulting weak form together with (3.3). This leads to the following primal-mixed variational form of the model problem written in terms of species concentration, deformation and pressure: *For any $t > 0$, find $(w_1(t), w_2(t), w_3(t), \mathbf{u}(t), p) \in H^1(\Omega_0) \times H^1(\Omega_0) \times H^1(\Omega_0) \times \mathbf{W}_D^{1,4}(\Omega_0) \times L^2(\Omega_0)$ satisfying*

$$[\mathscr{W}(w_1, w_2, w_3), (s_1, s_2, s_3)] = [\mathscr{H}(w_1, w_2, w_3), (s_1, s_2, s_3)], \quad (3.2)$$
$$(\partial_{tt}\mathbf{u}, \mathbf{v})_{0,\Omega_0} + [\mathscr{A}(\mathbf{u}), \mathbf{v}] = [\mathscr{G}(\mathbf{u}), \mathbf{v}], \quad (3.3)$$
$$[\mathscr{B}(\mathbf{u}), q] = 0, \quad (3.4)$$

for all $(s_1, s_2, s_3, \mathbf{v}, q) \in H^1(\Omega_0) \times H^1(\Omega_0) \times H^1(\Omega_0) \times \mathbf{H}_{D,0}^1(\Omega_0) \times L^2(\Omega_0)$, and where the non-linear operators associated with diffusion and reaction adopt the forms

$$[\mathscr{W}(w_1(t), w_2(t), w_3(t)), (s_1, s_2, s_3)] := \sum_{i=1}^{3} \left(\int_{\Omega_0} \partial_t w_i s_i + \int_{\Omega_0} \mathbf{F}^{-1}\mathbf{D_i}\mathbf{F}^{-t}\nabla w_i \cdot \nabla s_i \right),$$
$$[\mathscr{H}(w_1(t), w_2(t), w_3(t)), (s_1, s_2, s_3)] := \sum_{i=1}^{3} \int_{\Omega_0} H_i s_i + \int_{\Gamma_0^N} (H_3 + \delta_3 w_3)s_3,$$

Note that this formulation is quite general, as it is independent of the constitutive equations for the hyperelasticity, of the specific growth model, and of the reactive kinetics of the

system. The well-definiteness of the variational formulation requires special assumptions on the regularity of the specific coefficients and on the properties of the involved non-linear operators (such as Lipschitz continuity, monotonicity, ellipticity, compactness, and so on). Dedicated studies on the unique solvability of (3.3)-(3.4) are not yet available, however related results concerning the coupling of linear elasticity and reaction-diffusion systems have been addressed in the context of cardiac and plant cell biomechanics [3, 38].

In what follows we provide the Rothe-type strategy employed: we first apply a time discretization based on finite differences, followed by the specification of the primal-mixed finite element method.

3.1.1 Time discretization

The time-advancing method we choose here considers a uniform partition of the time interval $[0, T]$ as $\left[0, \ldots, t^n, \ldots, t^N = T\right]$ into N subintervals of size Δt. We simply adopt the implicit Euler scheme and central difference marching schemes as specified below. This implies that the method is fully implicit and therefore we obtain a non-linear semi-discrete problem as follows: For given values of $w_i^0, \mathbf{u}^0, \mathbf{u}^{-1}, p^0$ and for $n = 0, 1, \ldots$, find $\left(w_1^{n+1}, w_2^{n+1}, w_3^{n+1}, \mathbf{u}^{n+1}, p^{n+1}\right)$ such that

$$\sum_{i=1}^{3} \frac{1}{\Delta t} \left(\dot{w}_i^{n+1}, s_i\right)_{\Omega_0} + \left(\mathbf{F}^{-1}\mathbf{D_i}\mathbf{F}^{-t}\nabla w_i^{n+1}, \nabla s_i\right)_{\Omega_0} = [\mathscr{H}(w_1^{n+1}, w_2^{n+1}, w_3^{n+1}), (s_1, s_2, s_3)],$$

$$(3.5)$$

$$\frac{1}{(\Delta t)^2} \left(\ddot{\mathbf{u}}^{n+1}, \mathbf{v}\right)_{\Omega_0} + [\mathscr{A}(\mathbf{u}^{n+1}, p^{n+1}), \mathbf{v}] = [\mathscr{G}(\mathbf{u}^{n+1}), \mathbf{v}], \tag{3.6}$$

$$[\mathscr{B}(\mathbf{u}^{n+1}), q] = 0, \tag{3.7}$$

for all $(s_1, s_2, s_3, \mathbf{v}, q) \in \mathrm{H}^1(\Omega_0) \times \mathrm{H}^1(\Omega_0) \times \mathrm{H}^1(\Omega_0) \times \mathbf{H}_{\mathrm{D},0}^1(\Omega_0) \times \mathrm{L}^2(\Omega_0)$, where the dot and double dot symbols denote implicit Euler and central difference scheme for the time discretization of the first and second order time derivatives, respectively, i.e.,

$$\dot{s}^{n+1} := s^{n+1} - s^n,$$
$$\ddot{\mathbf{v}}^{n+1} := \mathbf{v}^{n+1} - 2\mathbf{v}^n + \mathbf{v}^{n-1}.$$

The time marching scheme is unconditionally stable, which allows in particular to take large time steps without compromising stability. For the 3D examples in the manuscript we have used semi-implicit methods instead, where the reactions are taken at the time iteration n.

However CFL-like restrictions are not needed since the diffusion approximations are still implicit.

3.1.2 Space discretization

Let us denote by $\mathscr{T}_h$ a regular simplicial partition of Ω_0 by triangles K of diameter h_K and define the meshsize as $h := \max\{h_K : K \in \mathscr{T}_h\}$. As usual, $\mathbb{P}_r(R)$ denotes the space of polynomial functions of degree $s \leq r$ defined on the set R. We seek a piecewise quadratic approximation of displacement, and Lagrangian finite element approximations for pressure and the three morphogen concentrations. The corresponding finite-dimensional trial spaces $\mathbf{W}_h \subset \mathbf{W}^{1,4}(\Omega), S_h \subset \mathrm{L}^2(\Omega)$ are defined in the general case of arbitrary order $k \geq 0$, as follows:

$$\mathbf{W}_h := \left\{ \mathbf{v}_h \in \mathbf{C}^0(\Omega) : \mathbf{v}_h|_K \in \mathbb{P}_{k+1}(K)^d, \forall K \in \mathscr{T}_h, \quad v_h|_{\Gamma^D} = g_D \right\},$$
$$S_h := \left\{ q_h \in \mathrm{L}^2(\Omega) : q_h|_K \in \mathbb{P}_k(K), \forall K \in \mathscr{T}_h \right\},$$

and the test space is

$$\mathbf{V}_h := \left\{ \mathbf{v}_h \in \mathbf{C}^0(\Omega) : \mathbf{v}_h|_K \in \mathbb{P}_{k+1}(K)^d, \forall K \in \mathscr{T}_h, \quad v_h|_{\Gamma^D} = 0 \right\}.$$

For the numerical results produced in this document we have restricted ourselves to the case of $k = 1$, which for the hyperelasticity equations corresponds to the Taylor-Hood pair (see Figure 3.1). Then using these spaces, the Galerkin method associated with the nonlinear
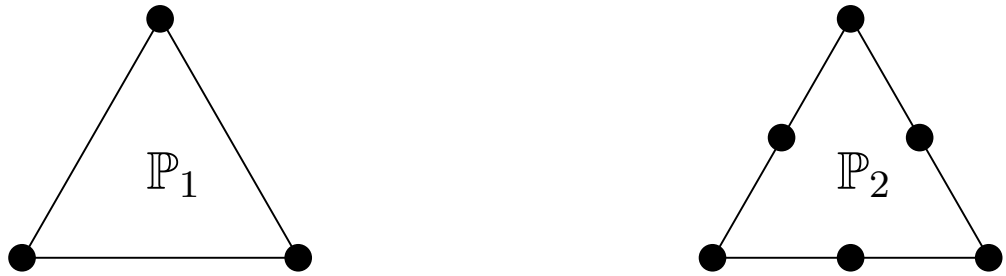
Fig. 3.1 Representation of degrees of freedom for the finite element spaces $\mathbb{P}_1$ and $\mathbb{P}_2$ on a given triangular element.

discrete-in-time system (3.5)-(3.7) can be written as

$$
\sum_{i=1}^{3} \frac{1}{\Delta t} \left(\dot{w}_{i,h}^{n+1}, s_{i,h} \right)_{\Omega_0} + \left(\mathbf{F}^{-1} \mathbf{D_i} \mathbf{F}^{-t} \nabla w_{i,h}^{n+1}, \nabla s_{i,h} \right)_{\Omega_0} = [\mathscr{H}(w_{1,h}^{n+1}, w_{2,h}^{n+1}, w_{3,h}^{n+1}), (s_{1,h}, s_{2,h}, s_{3,h})],
$$

$$
\frac{1}{(\Delta t)^2} \left(\ddot{u}_h^{n+1}, \mathbf{v}_h \right)_{\Omega_0} + [\mathscr{A}(u_h^{n+1}, p_h^{n+1}), \mathbf{v}_h] = [\mathscr{G}(u_h^{n+1}), \mathbf{v}_h],
$$

$$
[\mathscr{B}(u_h^{n+1}), q_h] = 0,
$$

for all $\left(s_{1,h}, s_{2,h}, s_{3,h}, \mathbf{v_h}, q_h \right) \in S_h \times S_h \times S_h \times \mathbf{V}_h \times S_h$ and for each $n = 0, 1, \dots$ Whenever clear from the context, we will drop the superscript $n+1$ corresponding to the current time step.

3.2 Linearisation of the problem

The solution of the set of nonlinear equations that one encounters at each time step proceeds by the Newton-Raphson method. Choosing as an initial guess the solution obtained at the previous time iteration

$$
(\mathbf{u}_h^{k=0}, p_h^{k=0}, w_{1,h}^{k=0}, w_{2,h}^{k=0}, w_{3,h}^{k=0}) = (\mathbf{u}_h^n, p_h^n, w_{1,h}^n, w_{2,h}^n, w_{3,h}^n),
$$

for $k = 0, 1, \dots$, we must find a sequence of approximate incremental displacement (that satisfies an homogeneous essential boundary condition), pressure, and three chemical concentrations $(\delta \mathbf{u}_h^{k+1}, \delta p_h^{k+1}, \delta w_{1,h}^{k+1}, \delta w_{2,h}^{k+1}, \delta w_{3,h}^{k+1})$ such that

$$
\overline{\mathscr{A}} \left[\delta \mathbf{u}_h^{k+1}, \mathbf{v}_h \right] + \mathscr{A}_1 \left[\delta \mathbf{u}_h^{k+1}, \mathbf{v_h} \right] + \overline{\mathscr{B}} \left[\delta p_h^{k+1}, \mathbf{v_h} \right] = \overline{\mathscr{G}} \left(\delta \mathbf{u}_h^{n+1}, \mathbf{v}_h \right) + F_1 \left(\mathbf{v_h} \right),
$$

$$
\overline{\mathscr{B}} \left(q_h, \delta \mathbf{u}_h^{k+1} \right) = F_2 \left(q_h \right), \tag{3.8}
$$

$$
\overline{\mathscr{C}} \left(\delta w_{1,h}^{k+1}, \delta w_{2,h}^{k+1}, \delta w_{3,h}^{k+1}, s_{1,h}, s_{2,h}, s_{3,h} \right) = F_3 \left(s_{1,h}, s_{2,h}, s_{3,h} \right),
$$

for all $\left(s_{1,h}, s_{2,h}, s_{3,h}, \mathbf{v_h}, q_h\right) \in S_h \times S_h \times S_h \times V_h \times S_h$ and where

$$\overline{\mathscr{A}} = \int_{\Omega_0} \frac{\delta \mathbf{u}_h^{k+1}}{\Delta t^2} \cdot \mathbf{v}_h,$$

$$\mathscr{A}_1 = \int_{\Omega_0} (\nabla \delta \mathbf{u}_h^{k+1} \mu \det(\mathbf{F_g}^k)(\mathbf{F}_g^k)^{-1}(\mathbf{F}_g^k)^{\mathsf{t}} : \nabla \mathbf{v}_h + p^k J((\mathbf{F}^k)^{-1} \nabla \delta \mathbf{u}_h^{k+1})^{\mathsf{t}} : (\mathbf{F}^k)^{-1} \nabla \mathbf{v}_h),$$

$$\overline{\mathscr{B}}(p, \mathbf{v}) = -\int_{\Omega_0} p J (\mathbf{F}^k)^{-\mathsf{t}} : \nabla \mathbf{v},$$

$$\overline{\mathscr{G}} = -\int_{\Gamma_0^N} (J(\mathbf{F^k})^{-\mathsf{t}}(\delta(\mathbf{u}_h^{k+1})^{\mathsf{t}}(\mathbf{F^k})^{-\mathsf{t}} \mathbf{t} \cdot \mathbf{v}_h - J(\mathbf{F^k})^{-\mathsf{t}} \mathbf{t} \cdot \mathbf{v}_h),$$

$$\overline{\mathscr{C}} = \sum_{i=1}^{3} \left(\frac{1}{\Delta t} \left(\delta w_{i,h}^{k+1}, s_{i,h} \right)_{\Omega_0} + \int_{\Omega_0} \left(\mathbf{F}^k \right)^{-1} \mathbf{D_i} \left(\mathbf{F}^k \right)^{-\mathsf{t}} \nabla \delta w_i^{k+1} \cdot \nabla s_i - \int_{\Omega_0} \frac{\partial H}{\partial w_i} \delta w_i^{k+1} s_{i,h} \right),$$

$$F_1(\mathbf{v_h}) = \int_{\Omega} \mathbf{R}_u^k \cdot \mathbf{v_h},$$

$$F_2(q_h) = \int_{\Omega} R_p^k \cdot q_h,$$

$$F_3\left(s_{1,h}, s_{2,h}, s_{3,h}\right) = \int_{\Omega} R_{\mathbf{w}}^k \cdot q_h.$$

Here we use the relation

$$D\mathbf{F}^{-T}(\mathbf{u}) = -\mathbf{F}^{-T}(\mathbf{u})^T \mathbf{F}^{-T}, \quad DJ(\mathbf{u}) = J\mathbf{F}^{-T} : \nabla \mathbf{u}$$

for all $\mathbf{u}$, and $\mathbf{R}_u^k$ is a vector residual and $R_{\mathbf{w}}^k, R_p^k$ are scalar residuals associated with the Newton-Raphson linearisation having quantities pertaining to the previous iteration. We then perform an update

$$\mathbf{u}^{k+1} = \mathbf{u}^k + \delta \mathbf{u}^{k+1},$$

$$p^{k+1} = p^k + \delta p^{k+1},$$

$$w_i^{k+1} = w_i^k + \delta w_i^{k+1}, \quad i = 1, 2, 3,$$

and continue with the iterations until the stopping criterion is met. Here we stop whenever the ℓ^2-norm of the discrete residuals or that of the relative residuals drops below a prescribed tolerance. Note that provided that the initial guess is sufficiently close to the updated solution, the use of the exact Jacobian ensures quadratic convergence of the Newton algorithm.

Finally, if we denote by U^{k+1}, P^{k+1}, W^{k+1} the vectors containing all degrees of freedom associated with the discrete incremental solutions δu_h^{k+1}, δp_h^{k+1} and $(\delta w_{1,h}^{k+1}, \delta w_{2,h}^{k+1}, \delta w_{3,h}^{k+1})$, then we can write the matrix system resulting from the tangent (Jacobian) problem as follows

$$\begin{pmatrix} \frac{1}{\Delta t^2} M_u U^{k+1} \\ 0 \\ \frac{1}{\Delta t^2} M_w W^{k+1} \end{pmatrix} + \begin{pmatrix} A_u & B^T & C_1^T \\ B^T & A_p & C_2 \\ C_1 & C_2 & A_w \end{pmatrix} \begin{pmatrix} U^{k+1} \\ P^{k+1} \\ W^{k+1} \end{pmatrix} = \begin{pmatrix} R_u \\ R_p \\ R_w \end{pmatrix},$$

where M_u and M_w denote the mass matrices associated with the finite element spaces $\mathbf{W}_h$ and $[S_h]^3$; A_u, A_p, A_w are the diagonal blocks of the linearized problem and B, C_1, C_2 contain all coupling terms still present after linearization.

Chapter 4

Numerical Results

In this section, we illustrate the performance of the mixed-primal finite element scheme in terms of convergence with respect to mesh size and time step and include representative examples. All results have been generated using the open-source finite element library FEniCS [2].

4.1 Accuracy test

In this section, we present the convergence results of our finite element scheme using the method of manufactured solutions. Let us consider the following manufactured solutions defined on the domain $\Omega = (0,1)^2$ as follows:

$$\mathbf{u}(x,y) = \begin{pmatrix} 0.5(sin(\pi x)cos(\pi y) + 0.5x^2)t^2, \\ -0.5(cos(\pi x)sin(\pi y) - 0.5y^2)t^2 \end{pmatrix}, \tag{4.1}$$

$$p = (x^3 - y^4)t, \tag{4.2}$$

$$w_1 = t(e^x + cos(\pi x)cos(\pi y)), \tag{4.3}$$

$$w_2 = t(e^{-y} + sin(\pi x)sin(\pi y)), \tag{4.4}$$

$$w_3 = t(cos(-x) + sin(\pi y)sin(\pi x)). \tag{4.5}$$

The forcing terms are calculated from these exact solutions and added to the weak formulation. We impose the homogeneous Dirichelet boundary conditions on $\mathbf{u}, w_1, w_2, w_3$, and the pure Neumann condition on the pressure p. Further constraints of zero average of the pressure, namely $\int_\Omega p dx = 0$, along with a Lagrange multiplier is added to the weak formulation to

					Space convergence					
h	$e_h(w_1)$	$r_h(w_1)$	$e_h(w_2)$	$r_h(w_2)$	$e_h(w_3)$	$r_h(w_3)$	$e_h(\mathbf{u})$	$r_h(\mathbf{u})$	$e_h(p)$	$r_h(p)$
0.7071	0.0656	–	0.0702	–	0.0668	–	6.989e-05	–	0.0410	–
0.3536	0.0358	0.8727	0.0356	0.9553	0.0362	0.9083	1.783e-05	1.9713	0.0217	0.9083
0.1768	0.0182	0.9696	0.0175	1.0470	0.0179	0.9924	4.038e-06	2.1421	0.0109	0.9924
0.0884	0.0092	0.9927	0.0086	1.0200	0.0090	0.9993	9.709e-07	2.0560	0.0055	0.9993
0.0442	0.0046	0.9982	0.0043	1.0060	0.0045	0.9999	2.399e-07	2.0172	0.0055	0.9999
0.0221	0.0023	0.9996	0.0021	1.0020	0.0022	1.0000	5.978e-08	2.0050	0.0014	1.0000

Table 4.1 Convergence test for the space discretization of the model problem.

ensure the uniqueness of pressure. Finally, we compute the errors between the exact and approximate solutions in H^1-norm for $\mathbf{u}, w_i$ and in the L^2-norm for p on a sequence of six uniformly refined meshes.

Space convergence

We begin with verifying the spatial convergence of the proposed numerical scheme. The absolute error and convergence rates are computed as

$$e_h(w) = w(\cdot, T) - w_h^N, r(x) = \frac{\log(e(x)/\tilde{e}(x))}{\log(h/\tilde{h})},$$

where e and $\tilde{e}$ denotes the errors generated on consecutive meshes of size h and $\tilde{h}$. These errors are computed using Gauss quadrature formulas, for the chosen approximation spaces, exact on each element. Here w_h^N represents the discrete approximation of the generic field w at the final time $t^N = T$. Table 4.1 reports the convergence history for the coupled problem, where convergence rates of $\mathcal{O}(h)$ are observed for w_1, w_2, w_3, p, while for the displacement $\mathbf{u}$ the convergence rate is of order $\mathcal{O}(h^2)$, suggesting our scheme our scheme reaches the expected convergence rate according to the interpolation properties of the employed linear Lagrangian element.

Time convergence

The accuracy of central difference and implicit Euler time discretization is also examined. Errors associated to the temporal discretization of a generic field w and convergence rate in

Time convergence								
Δt	$e_{\Delta t}(w_1)$	$r_{\Delta t}(w_1)$	$e_{\Delta t}(w_2)$	$r_{\Delta t}(w_2)$	$e_{\Delta t}(w_3)$	$r_{\Delta t}(w_3)$	$e_{\Delta t}(\mathbf{u})$	$r_{\Delta t}((\mathbf{u})$
0.5000	0.0314	–	0.0702	–	0.0668	–	8.284e-07	–
0.2500	0.0136	1.2092	0.0356	0.9553	0.0362	0.9083	4.145e-07	0.9988
0.1250	0.0063	1.1143	0.0175	1.047	0.0179	0.9924	2.069e-07	1.0030
0.0625	0.0031	1.0036	0.0086	1.0245	0.0090	0.9993	1.034e-07	1.0010
0.0313	0.0018	0.9982	0.0043	1.0063	0.0045	0.9999	5.194e-08	0.9932
0.0156	0.0013	0.9996	0.0021	1.0021	0.0022	1.0000	2.653e-08	0.9713

Table 4.2 Convergence test for the time discretization using central differences for the displacement and backward Euler for the reaction-diffusion system.

L^2-norm are calculated as follows:

$$e_{\Delta t}(w) = \sum_{n=0}^{N} \|w(\cdot, t^n) - w_h^n\|_2, \quad r_{\Delta t}(w) = \frac{\log\left(e_{\Delta t}(w)/\hat{e}_{\Delta t}(w)\right)}{\log(\Delta t/\widehat{\Delta t})},$$

on successively refined partition of the time interval. From Table 4.2, we evidence first order convergence rate for the time approximation of the problem when refining the timestep Δt, which achieves the results expected from the used approximation.

4.2 Validation of mechanical solver using benchmark

We next proceed to assess the numerical performance of the proposed hyperelastic constitutive model for the mechanical behaviour. Due to the inhomogeneous distribution of the growth factor in the limb, different parts of the tissue experience distinct growth rates. Such a differential growth may induce residual stress, which may, in turn, trigger the onset of instability. Therefore, in this section, we want to test the capability of our finite element code in investigating the onset of the instability in growing continua.

To do so, we consider the growth of a hollow disk with different thicknesses, following the work of Balbi and Cilartte [5]. The non-linear elastic formulation of the neo-Hooken model is given by (2.11)-(2.15), and a plane-strain condition is assumed. The external face is fixed while the free inner face is imposed a sinusoidal imperfection of prescribed mode m and amplitude $A = 0.05$, which is a common strategy used in the numerical simulation of this kind of problem. The solution is found through employing an incremental iterative Newton-Raphson method with a relaxation algorithm applied such that the code automatically adjusts the increment of the growth rate g if the Newton-Raphson method fails to converge.
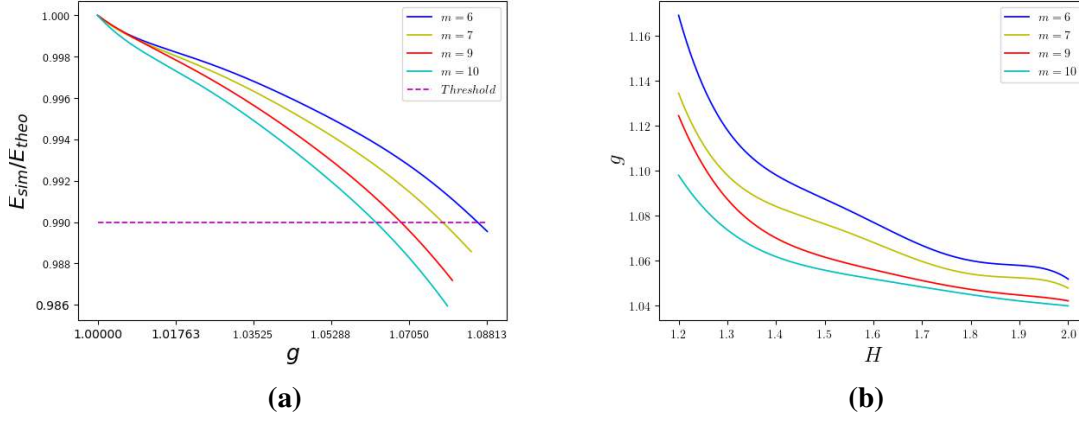
Fig. 4.1 Stability threshold for a growing hollow disk. (a) Energy ratio $E_{sim}/E_{theo} = 0.99$ against the growth factor g. (b) Approximated stability curves for different perturbation modes.

In each iteration, the calculation is performed using the linear algebra back-end PETSc and the system is solved by the GRMRES Krylov solver with an incomplete LU factorisation (ILUT) preconditioning. The stopping criterion on the non-linear iterations is based on a weighted residual norm dropping below the fixed tolerance of 1E−5.

We validate the numerical model by comparing the results from our code against the theoretical result presented in [5]. This is achieved by first computing the instability threshold for the growth factor. We identify the critical value g_{crit} as the value of the growth such that the ratio between the energy from the numerical solution, E_{sim}, and the theoretical axisymmetric energy, E_{theo}, is 0.99 ($E_{sim}/E_{theo} = 0.99$). Figure 4.1 (a) depicts the ratio E_{sim}/E_{theo} against the growth factor for different modes. The aspect ratio $H = R_o/R_i$ measures the thickness of the hollow disk, and the shear modulus is fixed at 2. The curves stop at critical points beyond which Newton solver fails to converge.

Once obtained these threshold growth rates, the marginal stability curve can be generated to validate against the theoretical stability curve. In Fig 4.1 (b), the critical growth value is presented against the aspect ratio and for different perturbation modes. This result achieves a good agreement with [5] for the occurrence of a surface instability mechanism. Although beyond the scope of this study, we present the behaviour in the fully non-linear region in Fig 4.2: after the emergence of the pattern, the amplitude of the wrinkles increases with the increasing growth factor g.

Finally, we remark that the mechanical solver is unable to capture the self-contact phenomenon, i.e., transition from a wrinkled to a creased state. A dedicated numerical scheme
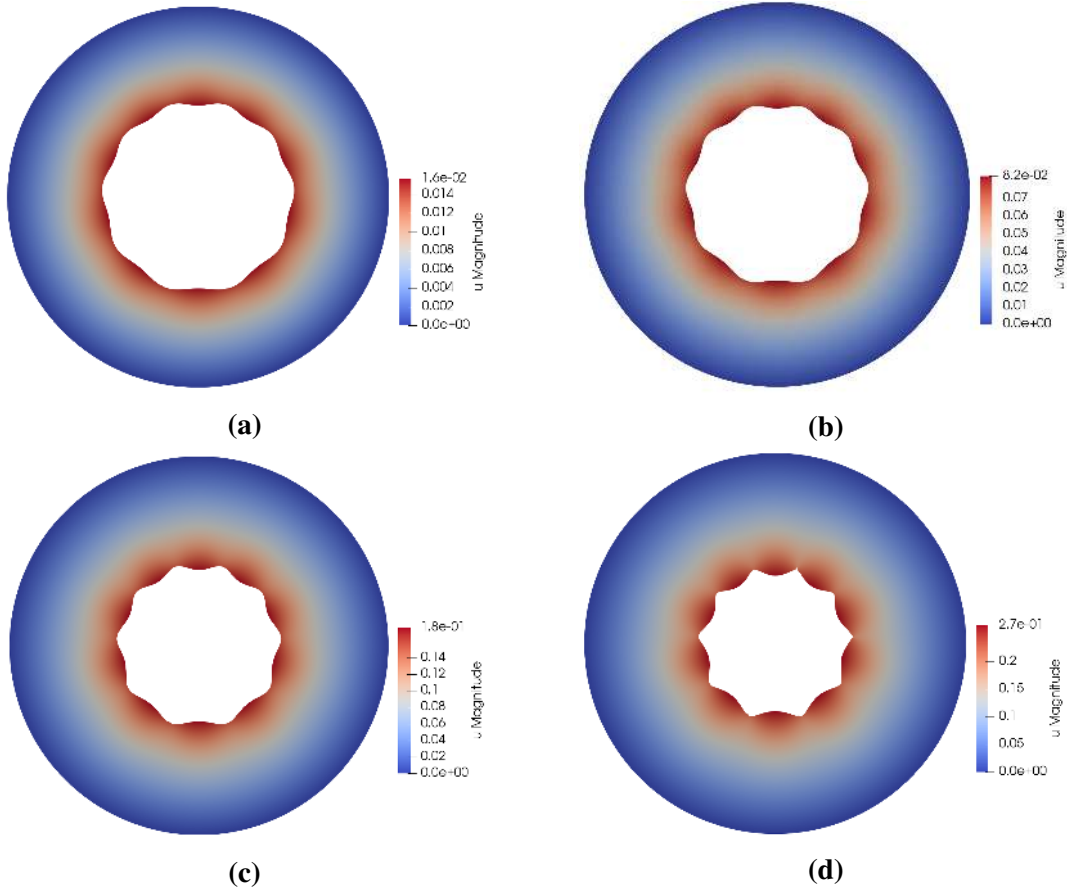
Fig. 4.2 Amplitude evolution of the initial perturbation of a growing hollow disk. The initial hollow disk is perturbed with the perturbation mode $m = 10$ and amplitude 0.05. The aspect ratio is fixed at 2 (a) $g = 1.05$, (b) $g = 1.025$, (c) $g = 1.05$, (d) $g = 1.07059$.

(e.g., pseudo-dynamic regularization, optimisation with constraint) would be needed. Growth-induced instabilities are a very active area of research, and we can mention for instance the developments in [6, 9, 12, 21]

4.3   Numerical simulations

In what is left of the section, the results are obtained by using the set of parameters prescribed in Section 2.1.3. Due to the multiphysics nature of the coupled problem, we run the simulations in the cycle that the chemical reaction takes place five times, providing the chemical prepattern, prior to the mechanical change in the free boundary in response to the chemically specified instruction.
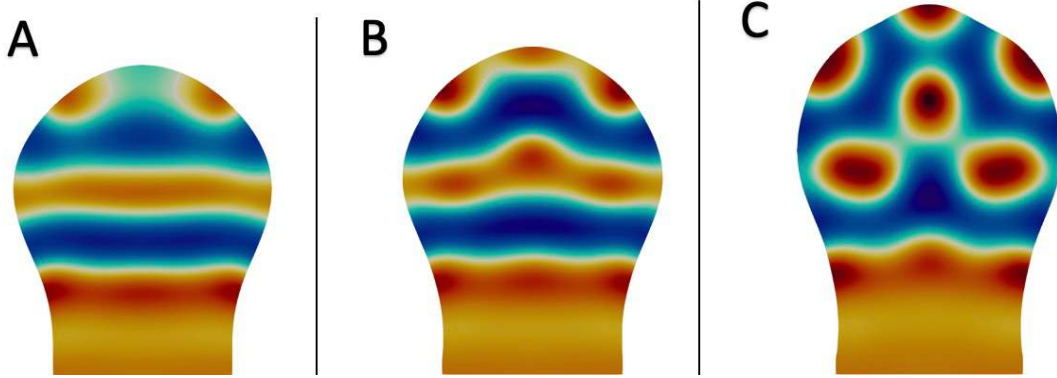
Fig. 4.3 The emergence of pattern on the growing domain of limb bud. The distribution of the BMP-receptor complex ($w_1 w_2^2$) at (A) $\tau = 200$, (B) $\tau = 600$, (C) $\tau = 800$.

## 4.3.1   Digit Patterning and Turing mechanism on the growing domain

As the marker for the tissue condensations isomorphic to the skeletal Digit-like structure, Sox9 expression is induced in response to BMP signalling. Therefore we expect the proposed Turing reaction-diffusion system modelling BMP signalling with the specified parameter choice will give rise to the pattern which faithfully mimics the distribution of SOX9. Fig 4.3 (A)-(C) exhibit the pattern of BMP-Receptor complex ($w_1 w_2^2$) that marks the regions of active BMP signaling and deems to resemble the SOX9 patterns observed in experiments. We observe that five spot-like patterns appear on the distal part of the growing domain, resembling the experimentally observed SOX9 patterns. Strong BMP signaling activity can be observed in the stalk. The sequence of spots emerges in the order 1,2,4,5/3 with digit 3 appears slightly later than other digits, whereas in the actual developing limb, digits appear in a sequence 4,2,3/1,5 [4]. One can notice the growth of the limb bud: the size of the domain in Fig 4.3 (A) is approximately 120% of its original size in Fig 4.3 (C). Here we assume that the growth process is slow and choose the linear growth rate by assuming the growth factor

$$\gamma_{w_1} w_2^2,$$

where the scaling parameter $\gamma \propto t$ will increase with time linearly and captures the domain growth rate. Under these conditions, the observed pattern is a quasi-steady state. If we increase the domain growth speed significantly by adjusting the scaling factor (e.g., quadratic growth), the pattern shows additional bifurcation of spots. The number of digits (patterns) depends on the domain growth speed, and the morphology of our model cannot evolve in a realistic growth rate (as fast as measured in the embryo), which is a similar situation to
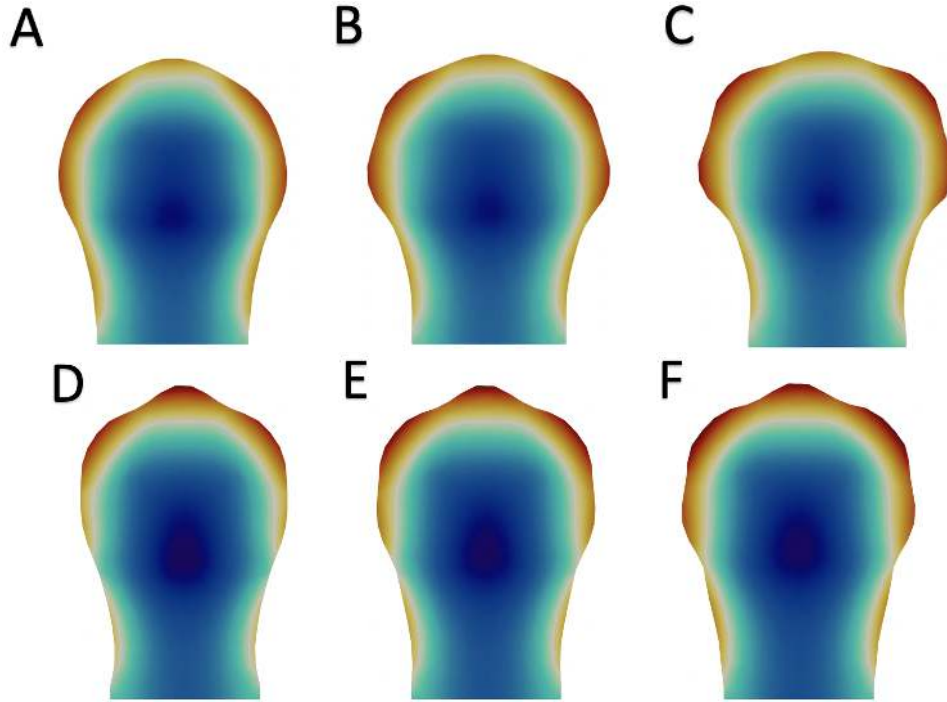
Fig. 4.4 Impact of the boundary condition and growth orientation on limb shaping.
(A)-(C) Isotropic growth is assumed. (A) $\delta_f = 0.002$, (B) $\delta_f = 0.01$, (C) $\delta_f = 0.018$. (D)-
(F) δ_f is fixed at 0.01 (D) $h = 0.4$, (E) $h = 1.0$, (F) $h = 1.6$. The concentration of FGF
experiences an abrupt increase on the AER with particular high values at the positions normal
to digits.

[4]. This suggests that more essential components of the regulatory interactions of BMP
signalling should be added to the reaction-diffusion system.

4.3.2 Boundary condition, growth orientation and limb shaping

In this section, we provide a descriptive explanation of how the proposed model gives rise to
desired limb shaping behaviour under certain conditions and compare it with some relevant
experimental results to support the model.

The formation of the limb shape is a mechanical process. One hypothesis that explains
the limb outgrowth stated that if the mesenchyme is "squeezed" by the ectoderm, the
general isotropic increase in volume could be converted into a distal elongation [13, 17].
An implication of this concept is that the mesenchyme exerts an outward force, which is
mechanically resisted by the ectoderm. As relevant experiment results showed that FGF
could act as a functional substitute for the apical ectodermal ridge responsible for growth

[45], we assume that the limb shaping and outgrowth are controlled by outward traction, the magnitude of which is determined by the proportion of the local concentration of FGF (δ_f), that is

$$[\mathbf{t}] \propto \delta_f w_3.$$

From Fig 4.4 (A)-(C), we can observe the following: First, the concentration of FGF experiences an abrupt increase on the apical ectodermal ridge. Second, the magnitude of the traction is a critical condition to determine the desired deformation of the distal end of the limb. Fig 4.4 (B) is a base case in which δ_f is 0.01, while the other panels (A), (C) demonstrates the effect of varying this coefficient — Decreasing δ_f leads to a more flattened handplate, whereas increasing δ_f leads to apparent wrinkles on the distal end of the handplate; When δ_f surpasses the threshold, Newton solver diverges and will not be able to generate more finger-like fold on the margin of the handplate.

Growth orientation is another critical condition to influence the limb shaping. Recall that the growth deformation gradient $\mathbf{F}_g$ is defined either isotropic

$$\mathbf{F}_g = r\mathbf{I},$$

or anisotropic

$$\mathbf{F}_g = \mathbf{I} + r_1 \mathbf{d}_1 \otimes \mathbf{d}_1 + r_2 \mathbf{d}_2 \otimes \mathbf{d}_2,$$

where $\mathbf{d}_1$ and $\mathbf{d}_2$ are the horizontal and vertical direction, representing two most important axes, proximo-distal axes and antero-posterio axes, in the limb development respectively, and r_1, r_2 are the rates proportional to r. For the sake of simplicity, we assume $r_1 = r$, and $r_2 = hr$ and perform six simulations under the control parameter h ranging from 0.4 to 1.6. Fig 4.4 (D)-(F) demonstrates the limb shaping at $h = 0.4, 1, 1, 6$ at $\tau = 1200$. We found that when the growth is anterior-posterior axes biased, the distal end of the limb bud will be more flattened than the anterior-posterior end; By contrast, a proximo-distally biased growth induces a more visible distally directed limb bud elongation, as well as the deformation at the distal end.

We are now ready to validate our model against the experimental finding. Fig 4.5 (a)-(c), (g)-(i) is an empirical mouse limb developmental trajectory from [32] which accurately synthesizes extensive information about the real shape of the limb. The author employed a geometric morphometric technique to estimate the average shapes of a relatively large sample of the mouse embryo (over 864 images). The red lines indicate the shape that corresponds to the experimental averages for each age group. Simulation snapshots are shown in Fig 4.5 (d)-(f), (j)-(k). Comparing the experimental findings with our simulation results, we see an excellent agreement. Initially, (at $\tau = 200$, Fig 4.5 (d)), we first notice the BMP signalling
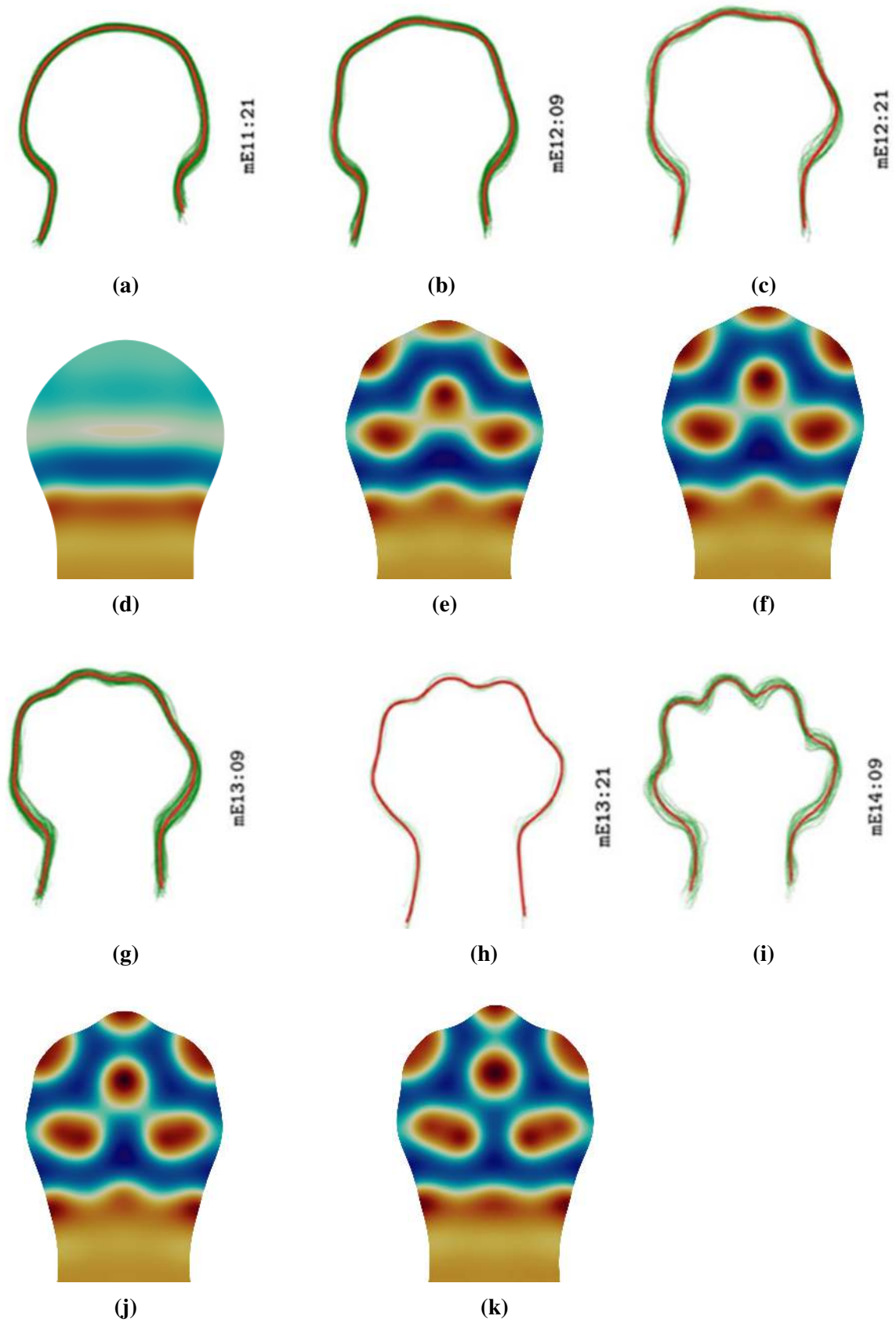
Fig. 4.5 Validation of the numerical simulation result against experimental data. (a)-(c), (g)-(i) Mouse limb bud growth trajectory, reprinted from [32]. (d)-(f),(j)-(k) Simulation snapshots of simulation results at (d) $\tau = 200$, (e) $\tau = 600$, (f) $\tau = 800$, (j) $\tau = 1000$, (k) $\tau = 1200$.

at the handplate, which corresponds to the experimental observation where the mesenchyme cells start to condense to form digits after E12; Within $\Delta\tau = 600$ (Fig 4.5 (e)), the distinct condensation can be discerned marked digits, which triggers the deformation of the distal end of the limb bud normal to the digit. After $\tau > 800$, one can visually recognize the initial appearance of a finger. However, due to the large deformation of the domain, after $\tau > 1400$ (Fig 4.5 (k)), the material model breaks down and Newton's solver fails to converge and so the pattern in Fig 4.5 (k) does not represent a stabilized final pattern.

4.4   Mechanical feedback: from spots to stripes

In this section, we explore the effects of the volume-dependent source terms acting as mechanical feedback into the reactions of the morphogens. The mechanical feedback on w_3 is neglected, since we observe that the abrupt increase in FGF essentially decouples the third equation from the core patterning mechanism governing by the first two equations in the reaction-diffusion system. Hence, we consider the modified right-hand sides for the first two species.

$$\tilde{H}_1 = H_1\left(w_1, w_2, w_3\right) + \zeta_1 \operatorname{div} \mathbf{u},$$
$$\widetilde{H}_2 = H_2\left(w_1, w_2, w_3\right) + \zeta_2 \operatorname{div} \mathbf{u},$$

where $\zeta_1, \zeta_2 \geq 0$. Similar terms have been employed in e.g., [33, 34]. The assumption underlying this choice is based on the idea of a simple positive loop. On the one hand, the inhomogeneous distribution of the morphogen will amplify the tissue growth. On the other hand, the corresponding morphological change of the tissue leads to a local displacement (stretch), which in turn induces the production of the morphogen locally.

With the presence of the mechanical feedback on the morphogens, the stability of the patterns originating from the basic reaction-diffusion system diminishes. The simulation initially shows patterns comparable to those observed in Fig 4.3 (A) (B). However, as the evolution of the limb shape continues, these patterns turn into a transient state. If the coupling parameter is chosen relatively small, spots bifurcate in the autopod region and gradually turn into quasi-steady state again after $\tau > 600$; If the coupling parameter ζ_2 is fixed at zero and ζ_1 is beyond a threshold (e.g. $\zeta_1 \approx 0.55$), the reaction of chemical morphogens will take place in a more intensive manner: the transient pattern will gradually evolve into stripes distributed at the autopod region of the limb bud. In Fig (a), we can see that the pattern achieves a better correspondence to the skeletal pattern than spot-like pattern generated from
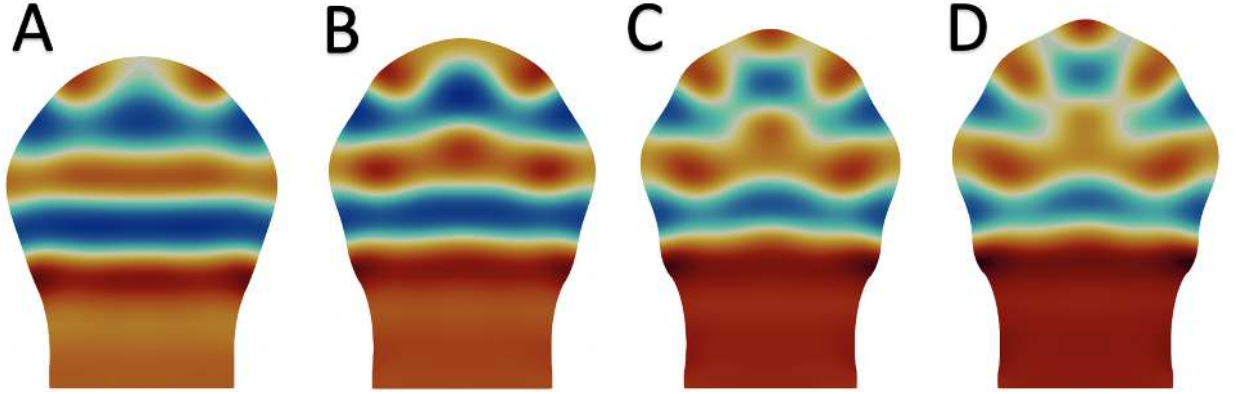
Fig. 4.6 Mechanical feedback on the pattern formation of morphogens Coupling parameter $\zeta_1 = 0.55, \zeta_2 = 0$. The distribution of the growth factor $(\gamma w_1 w_2^2)$ at (A) $\tau = 200$, (B) $\tau = 600$, (C) $\tau = 900$, (D) $\tau = 1000$.

a one-way coupled model, though the spot that represents the digit 3 does not fully connect to the remaining pattern to form a complete structure.

Overall, the process above shows that mechanical feedback plays an indispensable role in regulating the pattern formation of chemical morphogens. Moreover, to date, little research has been dedicated to understanding the mechanical influence of the limb morphology on the key regulatory interaction governing the skeletal pattern formation. Therefore, this finding of the transition from spots to the stripe-like patterns may shed light on the understanding of the biological mechanism underlying the formation of skeletal elements.

4.5   Anisotropic growth in 3D

For sake of illustration we finalise with a simple 3D test where we include two preferential directions for active deformation. The domain is a box of height 0.05 and side 1, that is $\Omega = (0,1) \times (0,1) \times (0,0.05)$, and we prescribe a growth deformation gradient of the form

$$\mathbf{F}_g = \mathbf{I} + \tau \left[t\mathbf{d}_1 \otimes \mathbf{d}_1 + t\mathbf{d}_2 \otimes \mathbf{d}_2 + \tau_3 w_1^2 \mathbf{d}_3 \otimes \mathbf{d}_3 \right]$$

where $\mathbf{d}_1, \mathbf{d}_2, \mathbf{d}_3$ coincide with the canonical basis in $\mathbb{R}^3$, and we put $\tau = 0.1$ and $\tau_3 = 0.4$. This implies that the active deformation due to linear growth and increasing linearly with time occurs in the horizontal directions whereas the active strain due to the chemical concentration will act on the x_3-direction. On the bottom surface we set zero normal displacements $\mathbf{u} \cdot \mathbf{n} = 0$
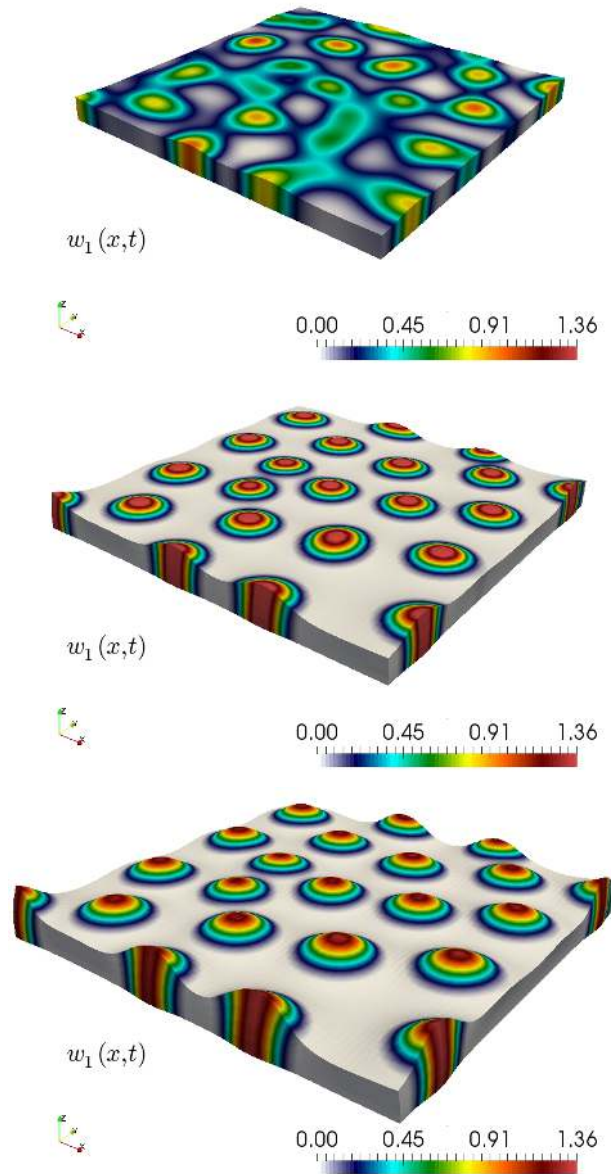
Fig. 4.7 Sample of concentrations of w_1 (top) at different times.

whereas on the remainder of the boundary we impose zero traction. For this test we have used a shear modulus of $\mu = 50$ and we depict the resulting patterns of concentration of w_1 on the deformed domain in Figure 4.7. We observe a gradual horizontal growth, much more marked than the bumps showing on the spatial spots.

Chapter 5

Concluding remarks

In summary, this thesis presents a coupled mechanochemical model for the embryonic development of mouse limb buds in using the theory of mechanical growth generalizing previous studies that imposed domain expansion solely in terms of morphogen growth factors. A simple linear analysis has been carried out, and a mixed-primal finite element scheme has been developed and thoroughly tested. We validated the simulation results against the experimental findings, which was rather promising: we observed not only the patterns of BMP-receptor activity that resembled the experimentally observed patterns for SOX9, but also a good correspondence of the morphology evolution to the mouse hindlimb development from E11.21 to 13:21.

We also explored the influence of the mechanical feedback on the morphogen dynamics by including the volume-dependent source terms into the reaction terms. The transition from spots to stripes was observed and the resulting pattern better mimicked the skeletal pattern than spot-like pattern obtained from a one-way coupled model. However, future work remains in order to fully understand the effect of mechanical feedback on the regulatory network of morphogens governing the formation of skeletal elements, as well as the morphology of the limb.

We believe that the present formalism is quite generic and can be broadly applied to similar contexts. We are currently working towards a few extensions that include exploring the need of viscoelastic effects and residual as well as initial stresses in producing more advanced developmental stages [10, 22], as well the generalization to other growth systems (different tissues and species) in mechanobiology [29, 42]; the reformulation of the equations of chemically-induced growth using strain, or stress (Kirchhoff or Piola-Kirchhoff tensors) as the main unknown [37]; analysing growth instabilities by looking at spectral properties of the

coupling mechanisms [20]; and the theoretical derivation of energy estimates establishing the stability of the time-dependent problem.

References

[1] Alawiye, H., Kuhl, E., and Goriely, A. (2019). Revisiting the wrinkling of elastic bilayers i: linear analysis. *Philosophical transactions. Series A, Mathematical, physical, and engineering sciences*, 377(2144).

[2] Alnæs, M. S., Blechta, J., Hake, J., Johansson, A., Kehlet, B., Logg, A., Richardson, C., Ring, J., Rognes, M. E., and Wells, G. N. (2015). The fenics project version 1.5. *Archive of Numerical Software*, 3(100).

[3] Andreianov, B., Bendahmane, M., Quarteroni, A., and Ruiz-Baier, R. (2015). Solvability analysis and numerical approximation of linearized cardiac electromechanics. *Mathematical Models and Methods in Applied Sciences*, 25(5):959–993.

[4] Badugu, A., Kraemer, C., Germann, P., Menshykau, D., and Iber, D. (2012). Digit patterning during limb development as a result of the bmp-receptor interaction. *Scientific Reports*, 2(1).

[5] Balbi, V. and Ciarletta, P. (2013). Morpho-elasticity of intestinal villi. *Journal of the Royal Society, Interface*, 10(82).

[6] Ben Amar, M. and Goriely, A. (2005). Growth and instability in elastic tissues. *Journal of the Mechanics and Physics of Solids*, 53(10):2284–2319.

[7] Boehm, B., Westerberg, H., Lesnicar-Pucko, G., Raja, S., Rautschka, M., Cotterell, J., Swoger, J., and Sharpe, J. (2010). The role of spatially controlled cell proliferation in limb bud morphogenesis (the role of proliferation in limb morphogenesis). *PLoS Biology*, 8(7).

[8] Brinkmann, F., Mercker, M., Richter, T., and Marciniak-Czochra, A. (2018). Post-turing tissue pattern formation: Advent of mechanochemistry. *PLoS computational biology*, 14(7).

[9] Ciarletta, P., Destrade, M., Gower, A., and Taffetani, M. (2016a). Morphology of residually stressed tubular tissues: beyond the elastic multiplicative decomposition. 90(C).

[10] Ciarletta, P., Destrade, M., Gower, A., and Taffetani, M. (2016b). Morphology of residually stressed tubular tissues: beyond the elastic multiplicative decomposition. 90(C).

[11] De Oliveira Vilaca, L. M., Milinkovitch, M. C., and Ruiz-Baier, R. (2019). Numerical approximation of a 3d mechanochemical interface model for skin patterning. *Journal of Computational Physics*, 384:383–404.

[12] Dervaux, J., Ciarletta, P., and Ben Amar, M. (2009). Morphogenesis of thin hyperelastic plates: A constitutive theory of biological growth in the föppl–von kármán limit. *Journal of the Mechanics and Physics of Solids*, 57(3):458–471.

[13] Dillon, R. and Othmer, H. G. (1999). A mathematical model for outgrowth and spatial patterning of the vertebrate limb bud. *Journal of Theoretical Biology*, 197(3):295–330.

[14] Ede, D. A. and Law, J. T. (1969). Computer simulation of vertebrate limb morphogenesis. *Nature*, 221(5177).

[15] Geuzaine, C. and Remacle, J.-F. (2009). Gmsh: A 3-D finite element mesh generator with built-in pre- and post-processing facilities. *International Journal for Numerical Methods in Engineering*, 79(11):1309–1331.

[16] Heisenberg, C.-P. and Bellaïche, Y. (2013). Forces in tissue morphogenesis and patterning. *Cell*, 153(5):948–962.

[17] Hornbruch, A. and Wolpert, L. (1970). Cell division in the early growth and morphogenesis of the chick limb. *Nature*, 226(5247).

[18] Howard, J., Grill, S. W., and Bois, J. S. (2011). Turing's next steps: the mechanochemical basis of morphogenesis. *Nature Reviews Molecular Cell Biology*, 12(6).

[19] Izaguirre, J. A., Chaturvedi, R., Huang, C., Cickovski, T., Coffland, J., Thomas, G., Forgacs, G., Alber, M., Hentschel, G., Newman, S. A., and Glazier, J. A. (2004). C ompu c ell , a multi-model framework for simulation of morphogenesis. *Bioinformatics*, 20(7):1129–1137.

[20] Javili, A., Dortdivanlioglu, B., Kuhl, E., and Linder, C. (2015). Computational aspects of growth-induced instabilities through eigenvalue analysis. *Computational Mechanics*, 56(3):405–420.

[21] Jones, G. W. and Chapman, S. J. (2012). Modeling growth in biological materials. *SIAM Review*, 54(1):52–118.

[22] Kida, N. and Morishita, Y. (2018). Continuum mechanical modeling of developing epithelial tissues with anisotropic surface growth. *Finite Elements in Analysis and Design*, 144:49–60.

[23] Kosher, R., Savage, M., and Chan, S. (1979). In vitro studies on the morphogenesis and differentiation of the mesoderm subjacent to the apical ectodermal ridge of the embryonic chick limb-bud. *Journal of embryology and experimental morphology*, 50:75–97.

[24] Kücken, M. (2004). Amodel for fingerprint formation. *EPL (Europhysics Letters)*, 68(1):141–146.

[25] Li, C., Xu, X., Nelson, D. K., Williams, T., Kuehn, M. R., and Deng, C.-X. (2005). Fgfr1 function at the earliest stages of mouse limb development plays an indispensable role in subsequent autopod morphogenesis. *Development (Cambridge, England)*, 132(21).

[26] Li, S. and Muneoka, K. (1999). Cell migration and chick limb development: Chemotactic action of fgf-4 and the aer. *Developmental Biology*, 211(2):335–347.

[27] Madzvamuse, A. and Maini, P. (2007). Velocity-induced numerical solutions of reaction-diffusion systems on continuously growing domains. *JOURNAL OF COMPUTATIONAL PHYSICS*, 225.

[28] Maini, P. K. and Solursh, M. (1991). Cellular mechanisms of pattern formation in the developing limb.

[29] Moreo, P., Gaffney, E., García-Aznar, J., and Doblaré, M. (2010). On the modelling of biological patterns with mechanochemical models: Insights from analysis and computation. *Bulletin of Mathematical Biology*, 72(2):400–431.

[30] Murea, C. and Hentschel, H. (2007). A finite element method for growth in biological development. *Mathematical biosciences and engineering : MBE*, 4:339–53.

[31] Murray, J. D. (2003). *Mathematical Biology. 3rd edition in 2 volumes: Mathematical Biology: II: Spatial Models and Biomedical Applications*. Springer.

[32] Musy, M., Flaherty, K., Raspopovic, J., Robert-Moreno, A., Richtsmeier, J. T., and Sharpe, J. (2018). A quantitative method for staging mouse embryos based on limb morphometry. *Development (Cambridge, England)*, 145(7).

[33] Neville, A., Matthews, P., and Byrne, H. (2006a). Interactions between pattern formation and domain growth. *Bulletin of Mathematical Biology*, 68(8):1975–2003.

[34] Neville, A., Matthews, P., and Byrne, H. (2006b). Interactions between pattern formation and domain growth. *Bulletin of Mathematical Biology*, 68(8):1975–2003.

[35] Oster, G. F., Murray, J. D., and Harris, A. K. (1983). Mechanical aspects of mesenchymal morphogenesis. *Journal of embryology and experimental morphology*, 78.

[36] Oster, G. F., Murray, J. D., and Maini, P. K. (1985). A model for chondrogenic condensations in the developing limb: the role of extracellular matrix and cell tractions. *Journal of embryology and experimental morphology*, 89.

[37] Propp, A., Gizzi, A., Levrero-Florencio, F., and Ruiz-Baier, R. (2019). An orthotropic electro-viscoelastic model for the heart with stress-assisted diffusion.

[38] Ptashnyk, M. and Seguin, B. (2016). Homogenization of a system of elastic and reaction-diffusion equations modelling plant cell wall biomechanics. *ESAIM. Mathematical Modelling and Numerical Analysis*, 50(2).

[39] Razavi, M. J., Pidaparti, R., and Wang, X. (2016). Surface and interfacial creases in a bilayer tubular soft tissue. *Physical review. E*, 94(2).

[40] Rodriguez, E. K., Hoger, A., and Mcculloch, A. D. (1994). Stress-dependent finite growth in soft elastic tissues. *Journal of Biomechanics*, 27(4):455–467.

[41] Ruiz-Baier, R. (2015). Primal-mixed formulations for reaction–diffusion systems on deforming domains. *Journal of Computational Physics*, 299(C):320–338.

[42] Socci, L., Pennati, G., Gervaso, F., and Vena, P. (2007). An axisymmetric computational model of skin expansion and growth. *Biomechanics and Modeling in Mechanobiology*, 6(3):177–188.

[43] Towers, M. and Tickle, C. (2009). Growing models of vertebrate limb development. *Development (Cambridge, England)*, 136(2).

[44] Wolpert, L. (1969). Positional information and the spatial pattern of cellular differentiation. *Journal of Theoretical Biology*, 25(1):1–47.

[45] Wolpert, L. (2001). *Principles of development*. Oxford University Press, Oxford, 2nd ed. edition.

[46] Zhang, Y.-T., Alber, M. S., and Newman, S. A. (2012). Mathematical modeling of vertebrate limb development. *Mathematical Biosciences*, 243(1).

[47] Zuniga, A. (2015). Next generation limb development and evolution: old questions, new perspectives. *Development (Cambridge, England)*, 142(22).